J Fluoresc (2015) 25:1063–1083
DOI 10.1007/s10895-015-1593-2

ORIGINAL ARTICLE

Site Specific Interaction Between TiO_2 Nanoparticles and Phenanthrimidazole—A First Principles Quantum Mechanical Study

Jayaraman Jayabharathi[1] · **Periyasamy Ramanathan**[1] · **Chockalingam Karunakaran**[1] · **Venugopal Thanikachalam**[1]

Received: 21 April 2015 / Accepted: 4 June 2015 / Published online: 26 June 2015

Abstract Understanding the interaction between the nanomaterials and bioactive molecules are of current interest due to the potential application of nanomaterial in biomedical field. The structural, electronic and optical properties of newly synthesised fluorophore 2-(4-methoxynaphthalen-1-yl)-1-phenyl-1H-phenanthro[9.10-d]imidazole have been investigated in detail. The imidazole absorbs strongly on the surface of TiO_2 nanocrystals probably because of the chemical affinity of azomethine nitrogen atom of the imidazole, resulting in lowering the HOMO and LUMO energy levels. The TEM, SEM and EDX spectra confirm the adsorption of imidazole on the surface of TiO_2 nanocrystals. The growth behavior and stability of small stoichiometric $(TiO_2)_n$ clusters have been analysed by using density functional theory which reveals that clusters prefers three-dimensional structures. In addition, the interaction between the ground state structure of the $(TiO_2)_n$ cluster and a single imidazole molecule have been studied. The calculated binding energy (E_b) and the energy gap (E_g) indicate that the imidazole molecule preferably binds to the Ti atom of the $(TiO_2)_n$ clusters through its azomethine nitrogen atom; the binding energy is in range 5.24–7.89 eV. In order to understand the binding interaction with DNA docking study has been carried out.

Keywords TiO_2 (A), TiO_2 (R), Phenanthrimidazole · TEM, SEM · EDX · XRD · DOS · HOMO-LUMO · Docking

Introduction

Titanium dioxide (TiO_2) has many promising applications because of its low cost, long-standing stability, catalytically active surfaces and environmental compatibility, production of hydrogen from water and solar energy, solar cells [1–8], sensors [9], cleaning of water and air from organic contaminants [10, 11] and photocatalysis [12–15]. The physical and chemical properties of TiO_2 nanomaterials, namely nanowires, nanoparticles and clusters, might be different from those of bulk titania [16]. The ratio of surface to volume atoms increases as the cluster size decreases; smaller TiO_2 nanoparticles have more active sites and so the catalytic activity of the TiO_2 materials is enhanced [17]. Due to their scientific and technological importance, there are several experimental [18–27] and theoretical studies on small neutral, negatively and positively charged TiO_2 clusters [28–48] and nanoparticles [49–52]. Structure, stability, electron affinities, harmonic vibrational frequencies of stoichiometric and non-stoichiometric neutral and charged clusters have been studied by employing density functional theory (DFT) based methods [36–44].

Arylimidazoles play important role in materials science and medicinal chemistry due to their optoelectronic properties and high thermal stabilities [53–57]. Substituted imidazoles are extensively used as glucagon receptors [58], cannabinoid receptor antagonists [59] and modulators of glycoprotein mediated multidrug resistance [60], antibacterial [61], anti-allergic [62], analgesic [63], antitumor [64] and pesticides [65]. Many of the reported synthetic protocols for imidazoles [66–73] suffer from disadvantages such as use of toxic and chlorinated

Electronic supplementary material The online version of this article (doi:10.1007/s10895-015-1593-2) contains supplementary material, which is available to authorized users.

✉ Jayaraman Jayabharathi
jtchalam2005@yahoo.co.in

[1] Department of Chemistry, Annamalai University, Annamalainagar 608 002, Tamilnadu, India

organic solvents, acidic conditions, complex work-up and purification, side reactions, low yield and use of hazardous and expensive reagents. Thus the development of a new catalyst is essential to overcome these shortcomings and to fulfill the criteria of a milder reaction conditions, higher yield and reusability of catalyst.

Adsorption of pyridine to large TiO_2 nanocrystals via carboxylic acid anchor group has been studied (C-site) [40, 74]. The interaction between the adsorbed bioactive organic molecules and TiO_2 surfaces, as well as the mechanism of the electron injection process is of current interest [74–81]. Because of the wide potential use of TiO_2 clusters it is essential to know their physical and chemical properties. For the first time, the binding of bioactive phenanthrimidazole with TiO_2 clusters has been analysed in terms of their size, binding energy, geometry, binding site, bond length and HOMO–LUMO energies. The experimental and theoretical results confirm the formation of ≥N– Ti bond in imidazole– TiO_2 composites (N-site). The overlap of d-orbital of titanium with azomethine nitrogen atom probably leads to a large binding energy for the N-site.

Experimental

Materials and Measurements

Phenanthroquinone, 4-methoxyaniline, 4-methoxynapthaldehyde and all other reagents have been purchased from Sigma-aldrich. NMR spectra were recorded on Bruker 400 MHz NMR spectrometer and the mass spectra of the samples were obtained using an Agilent LCMS VL SD in electron ionization mode. The UV–vis and photoluminescence spectra were recorded with Perkin Elmer Lambda 35 UV–vis spectrophotometer and PerkinElmer LS55 fluorescence spectrometer, respectively. The UV–vis diffuse reflectance spectra (DRS) were recorded with Perkin Elmer Lambda 35 spectrophotometer with RSA-PE-20 integrating sphere. Cyclic voltammetry (CV) and lifetime measurements were carried out with CHI 630A potentiostat electrochemical analyzer and Horiba Fluorocube-01-NL lifetime system with nano LED as the excitation source and TBX-PS as detector, respectively. The quantum yields were measured by comparing fluorescence intensities of a standard sample. Methanolic solution of imidazole of required concentration was mixed with the nanoparticles dispersed in methanol at different loading, after sonication, the absorption (1×10^{-5} M) and emission (1×10^{-8} M) spectra were recorded. TEM analysis was carried out using JEOL JEM 2100 high resolution transmission electron microscope (HR-TEM) with an accelerating voltage of 200 KV. X-ray diffraction (XRD) patterns were recorded for the centrifuged and dried samples using X–ray Rigaku diffractometer with Cu K_α source (30 kV, 100 mA), at a scan speed of 3.0000 deg/min, step width of 0.1000 deg, in a 2θ range of 20–80 . The energy dispersive X-ray spectra (EDX) of the nanosemiconductors were recorded with a JEOL JSM-5610 scanning electron microscope (SEM) equipped with back electron (BE) detector and EDX. The sample was placed on an adhesive carbon slice supported on copper stubs and coated with 10 nm thick gold using JEOL JFC- 1600 auto fine coater prior to measurement. Theoretical calculations were performed using Gaussian-03 program [82]. The electrostatic potential for each molecule is obtained by moving a unit positive point charge across the van der Waals surface and it is calculated at various points j on this surface using, $V_j=q_i/ r_{ji}$ Where q_i represents the partial charge of each atom i and r_{ji} is the distance between point's j and atom i. Starting from the 3D model of a molecule and its partial atomic charges, the electrostatic potential is calculated for points on the molecular surface.

Synthesis of 2-(4-Methoxynaphthalen-1-yl) -1-Phenyl-1H-Phenanthro[9.10-d]Imidazole

A mixture of 4-methoxy-1-naphthaldehyde (1 mmol), phenanthrene-9.10-dione (1 mmol), aniline (1 mmol) and ammonium acetate (1 mmol) with TiO_2 (1 mol%) as catalyst was stirred at 120 °C with continuous stirring with a bar magnet. The progress of the reaction was monitored by TLC (Scheme 1). After completion of the reaction, 10 mL ethyl acetate was added to the reaction mixture and shaken well to dissolve the organic components and the mass filtered to separate out TiO_2 and the residue was washed with ethyl acetate. The solid residue of TiO_2 was further washed with hot acetone and then dried up. The product was purified by column chromatography using benzene: ethyl acetate (9:1) as the eluent. The newly synthesised phenanthrimidazole have been characterised by ^1H and ^{13}C NMR and mass (MS) spectra. Yield: 75 %, M.p. 272 °C., Anal. calcd. for $C_{32}H_{22}N_2O$: C, 85.31; H, 4.92; N, 5.83. Found: C, 85.08; H, 4.82; N, 5.70. ^1H NMR (400 MHz, $CDCl_3$): δ 3.95 (s, 3H), 6.80 (d, J=8.8 Hz, 2H), 6.67 (d, J=8.0 Hz, 1H), 7.36 (d, J=8.0 Hz, 1H), 7.89 (d, J=6.8 Hz, 1H), 8.25 (d, J=6.8 Hz, 1H), 8.73 (d, J=8.0 Hz, 1H), 8.79 (d, J=8.4 Hz, 1H), 8.88 (d, J=8.0 Hz, 1H), 7.29 (t, J=6.4 Hz, 2H), 7.52 (t, 1H), 7.64 (t, 1H), 7.55 (t, 1H), 7.24–7.22 (m, 2H), 7.46–7.44 (m, 2H). ^{13}C NMR (400 MHz, $CDCl_3$): δ 55.54, 102.72, 114.61, 120.45, 121.01, 122.02, 122.89, 123.15, 124.10, 124.85, 125.42, 125.48, 125.79, 126.33, 127.23, 127.29, 127.46, 127.59, 128.27, 129.19, 129.54, 129.95, 130.84, 134.25, 137.17, 151.18, 156.40, 159.74. MS: m/z. 450.53 [M^+].

Scheme 1 Possible mechanism for catalytic synthesis of phenanthrimidazole

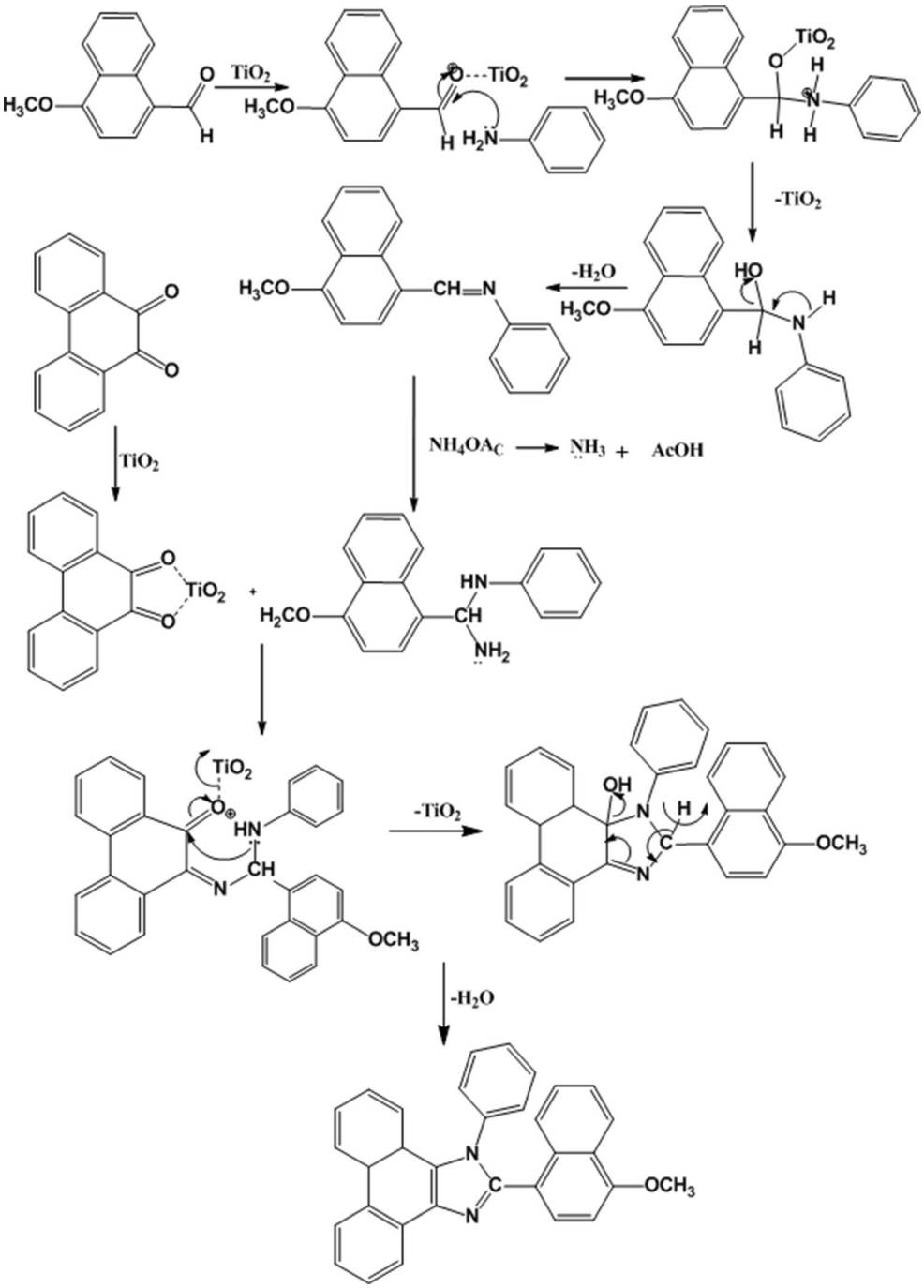

Synthesis of Nanocrystalline TiO_2 by sol–gel Method

The TiO_2 nanocrystal was synthesised by sol–gel hydrolysis of titanium (IV) isopropoxide, followed by calcination. About 1 mL of titanium isopropoxide (Merck, 97 %) was dissolved in 20 mL isopropyl alcohol (Merck, 95 %) and the solution was dropped slowly into 10 mL of distilled water, pH 2–6 was adjusted by 1 M HNO_3 for acidic condition and 1 M NaOH for basic condition. After stirring a mixture of water to alkoxide [Molar ratio 110] was added. The formed white sol–gel of hydrous oxide was stirred vigorously for 4 h at room temperature and then allowed to age overnight. The solid was centrifuged and was redispersed in ethanol to minimize agglomeration. This process was repeated for five times and the solid was filtered. The resulting material was then dried and calcinated at 400 and 600 °C for 2 h, respectively. The samples were characterised by XRD, SEM, EDX and TEM. From these results it is found that high acidity [pH 2] favor for the formation of rutile phase while lower acidity [pH 6] favour for anatase formation [83, 84].

Synthesis of Phenanthrimidazole-TiO_2 Composites

About 1 mmol of phenanthrimidazole in dimethyl sulphoxide (1 mL) was added to 1 mmol of TiO_2 (R) / TiO_2 (A) nanoparticles suspended in dimethyl sulphoxide (1 mL) under constant stirring for 3 h. The solid was filtered, washed with dimethyl sulphoxide and dried at 110 °C.

Molecular Docking Studies

The structure of ct-DNA is composed two strands that wrap around each other to form a right-handed double helix with the B-form. The crystal structure of B-DNA [(CGCGAATTCG CG)$_2$] is used in molecular docking were extracted from Protein Data Bank (http://www.rcsb.org/pdb). MGL tools 1. 5.4 with AutoGrid4 and AutoDock4 were used to perform the docking calculations between the 2-(4-methoxynaphthalen-1-yl)-1-phenyl-1H-phenanthro[9.10-d]imidazole and DNA sequence. Crystal structure of 2-(4-methoxynaphthalen-1-yl)-1-phenyl-1H-phenanthro[9.10-d]imidazole was saved in MOL file and used for docking. Receptor (DNA) and 2-(4-methoxynaphthalen-1-yl)-1-phenyl-1H-phenanthro[9.10-d] imidazole (drug) files were provided using AutoDock Tools. All of the hetero atoms, water molecules and other unwanted ions were removed from B-DNA using Discovery Studio 4.0 [85]. The polar hydrogen atoms, partial atomic charges and Gasteiger charges of DNA were added to the compound by AutoDock Tools [86, 87] before subjecting to docking analysis. Ligand docking calculations were carried out using Lamarckian genetic algorithm (LGA) [88]. The DNA molecule was enclosed in a box with number of grid points of 126× 126×126 was created along the x, y and z axis and a grid spacing of 0.375 Å, i.e., blind docking was performed. The output structures of the docked molecules were further analyzed with PyMOL software package [89].

Results and Discussion

Nanocrystalline anatase and rutile phases of TiO_2 was obtained by sol–gel method, characterized by XRD, SEM, TEM and EDX, UV–visible diffuse reflectance and solid state photoluminescence spectroscopies. We examine the photoelectron transfer (PET) from photoexcited imidazole to TiO_2 (A) and TiO_2 (R) and find that the imidazole can be used to differentiate the rutile phase of TiO_2 from anatase phase.

Characterisation of TiO_2 (R) and TiO_2 (A) Nanocrystals

XRD pattern of both anatase and rutile phases of TiO_2 nanoparticles are shown in Fig. 1. The diffraction patterns of TiO_2 (A) and TiO_2 (R) matches with the standard JCPDS pattern of anatase (89–4921), body centered tetragonal with crystal constants a=b =3.7774A° and c=9.501 Å and (89–4920) with crystal constants a and b as 4.584A° and c as 2.953 Å, respectively. The average crystallite sizes (D) of the TiO_2 (A) and TiO_2 (R) have been obtained as 11.4 and 27.2 nm, respectively, by using the Scherrer equation, $D=0.9\,\lambda/\beta\cos\theta$, [$\lambda$ is the wavelength of the X-ray used, θ is the diffraction angle and β is the full width at half maximum of the peak]. The specific surface area (S) of the nanocrystals have been deduced by using the relationship $S=6/\rho D$ (ρ is the material density). The calculated surface areas for anatase and rutile phases of TiO_2 are 135 and 38.8 m^2/g, respectively. The large increase in crystal size of rutile TiO_2 results in a large decrease of surface area. The SEM images and EDX spectra of TiO_2 (A) and TiO_2 (R) nanoparticles are displayed in Fig. 2. The EDX spectra of TiO_2 (A) and TiO_2 (R) nanoparticles are displayed in Fig. 2. Absence of peaks other than titanium and oxygen reveal the purity of the samples.

Optical Properties

Figure 3 shows the diffuse reflectance spectra (DRS) of sol–gel synthesized anatase and rutile TiO_2. They are presented in terms of $F(R)$, deduced from the recorded reflectance (R) by application of the Kubelka-Munk algorithm [$F(R)=(1-R)^2/2R$]. The absorption edges of rutile and anatase TiO_2 are 379 and 343 nm respectively. The deduced absorption edges provide the band gap of anatase and rutile TiO_2 as 3.26 and 3.61 eV, respectively. The observed band gaps are in agreement with the mean crystalline sizes of the synthesised TiO_2 (A) and TiO_2 (A) nanoparticles. The band gap of anataseTiO_2 is larger than reported value (3.2 eV) [90]. This is because the smaller size of the synthesized nanoparticles: the size of the nanoparticle is about 11 nm. Similarly the band gap of the synthesised rutile TiO_2 is larger than the literature value. This is also because of the smaller size of the synthesized nanoparticles. Quantum confinement effect increases the band gap energy.

The solid state photoluminescence spectra of the anatase and rutile TiO_2 nanocrystals. The rutile TiO_2 exhibit prominent emission at 378 and 403 nm, when excited at 340 nm. The shorter wavelength corresponds to the band gap emission and the longer one is because of crystal defects. The solid emission spectra of rutile TiO_2 and anatase TiO_2 mainly display four emission bands: a strong violet emission at 415 nm (2.99 eV), a blue band at 451 nm (2.75 eV), a blue-green band at 483 nm (2.56 eV), and a weak green band at 526 nm (2.34 eV). The emissions at 476 and 520 nm are assigned to the transition from the oxygen vacancies with two trapped electrons and one trapped electron to the valence band of TiO_2, respectively. The energy levels corresponding to two kinds of the oxygen vacancies are located at 0.51 and 0.82 eV below the conduction band (CB) of TiO_2,

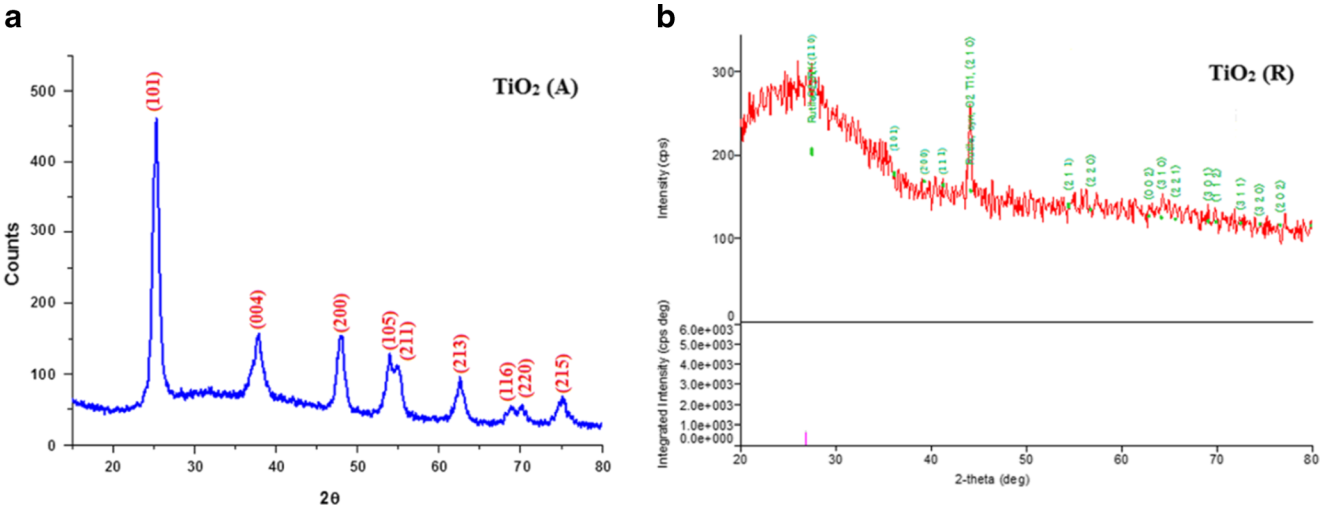

Fig. 1 X-ray diffraction patterns (XRD) of (**a**) TiO_2 (A); (**b**) TiO_2 (R)

respectively. Because of the presence of the energy levels of oxygen vacancies, first the photogenerated electrons in the CB is likely to reach the oxygen vacancies through a non-radiative process and then recombine with the photogenerated holes in the valence band (VB) followed by the emission of fluorescence. The observed broad band at 440–483 nm (2.56−2.81 eV) in the visible region is also assigned to the radiative recombination of excitons of the shallow traps identified with oxygen vacancies and Ti^{4+} adjacent to oxygen vacancies [91].

Characterization of Nano Imidazole-TiO_2 (R) and Imidazole-TiO_2 (A) Composites

Figure 4 displays the XRD pattern of both imidazole-TiO_2 (A) and imidazole-TiO_2 (R) composites. The diffraction pattern of imidazole-TiO_2 (A) composite match with the standard JCPDS pattern of body centered tetragonal anatase (89–4921) with crystal constants a=b =3.7774A° and c= 9.501 Å. The diffraction pattern of imidazole-TiO_2 (R) composite matches with the JCPDS pattern of tetragonal (89–

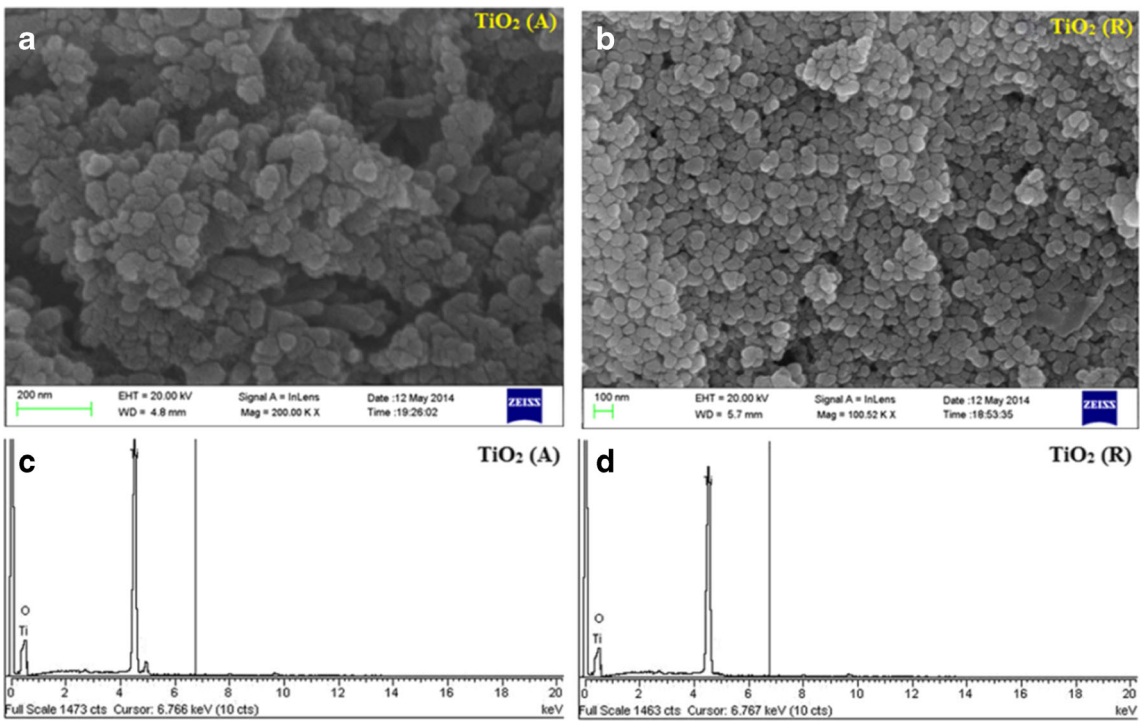

Fig. 2 SEM images of (**a**) TiO_2 (A); (**b**) TiO_2 (R); EDX spectra of (**c**) TiO_2 (A); (**d**) TiO_2 (R)

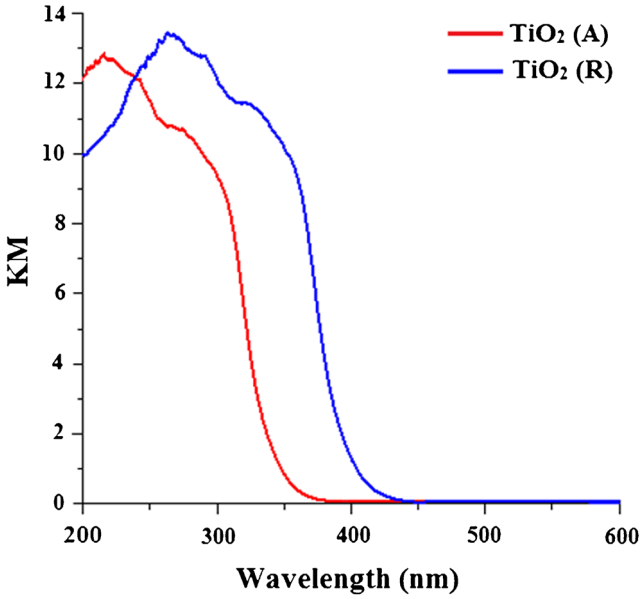

Fig. 3 Diffused reflectance spectra of TiO_2 (A) and TiO_2 (R)

4920). The crystal constants a or b and c are 4.584 and 2.953 Å, respectively. The average crystallite sizes (D) of the composites have been deduced by using the Scherrer equation as 17.6 and 27 nm respectively.

The calculated surface areas of imidazole-TiO_2 (A) and imidazole-TiO_2 (R) composites are 87 and 36.2 m^2/g, respectively. The slight increase in crystal size of imidazole-TiO_2 (R) composites results in a small decrease of surface area. The SEM images and EDX spectra of imidazole-TiO_2 (A) and imidazole-TiO_2 (R) composites (Fig. 5) and the TEM images are displayed in Fig. 6. The SEM images show that adsorption of imidazole significantly modifies the morphology of the TiO_2 nanocrystal. The EDX spectra of imidazole-TiO_2 composites confirm the adsorption of imidazole on TiO_2 nanocrystalline surface. The TEM images confirm that they are nanoparticles and the measured crystallite size agrees with that obtained by XRD.

Ground State Interaction Between Imidazole and TiO_2 Nanoparticles

The three absorption bands at 257, 233 and 305 nm are assigned to $^1(\pi - \pi^*)$ transition corresponding to Platt's

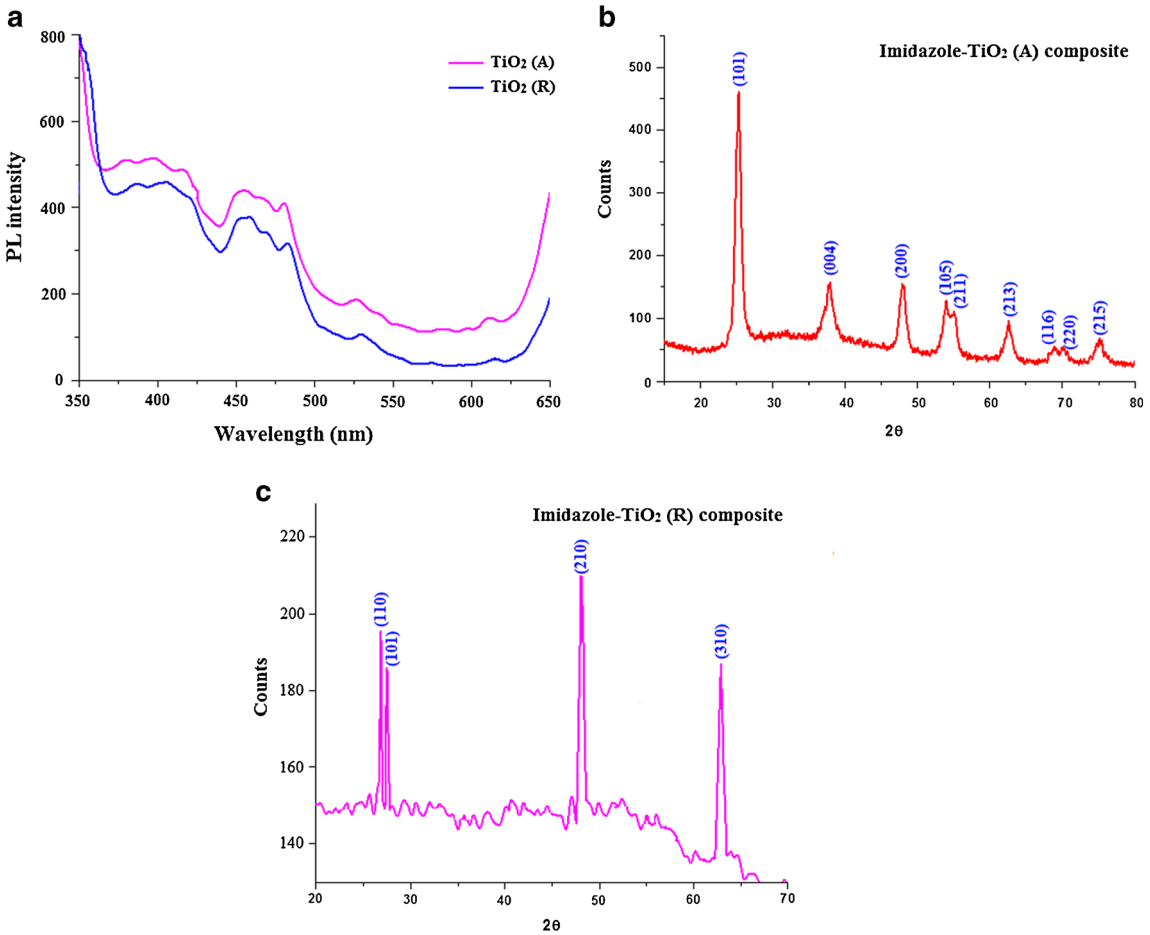

Fig. 4 **a** Solid photoluminescence spectra of TiO_2 (A) and TiO_2 (R); X-ray diffraction patterns (XRD) of **b** imidazole-TiO_2 (A) composite and **c** imidazole-TiO_2 (R) **c** composite

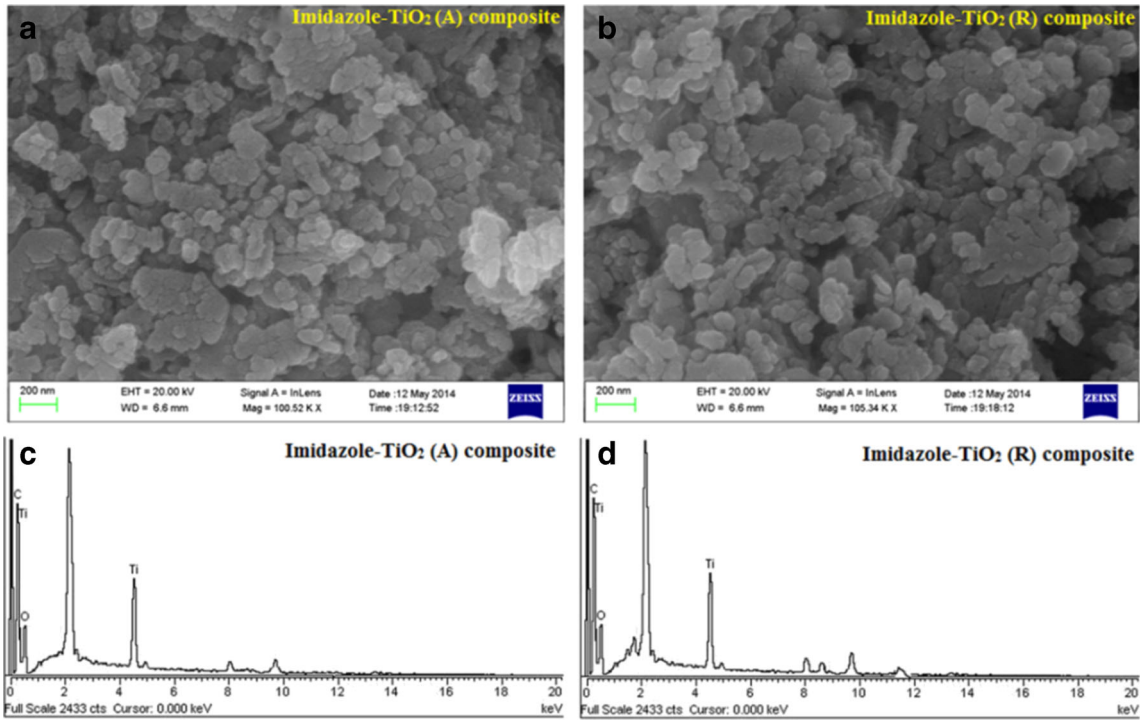

Fig. 5 SEM images of (**a**) imidazole-TiO_2 (A) composite and (**b**) imidazole-TiO_2 (R) composite; EDX spectra of (**c**) imidazole-TiO_2 (A) composite and (**d**) imidazole-TiO_2 (R) composite

notations ^1L_b, ^1L_a and ^1B_a in the excited states. The low and high energy transitions, $^1L_b \leftarrow S_0$, $^1L_a \leftarrow S_0$ and $^1B_a \leftarrow S_0$, respectively are observed in the absorption spectra [92, 93]. The superpositions of the bands corresponding to the donor and acceptor subunits are only slightly perturbed by their interactions. The low-energy absorption region of the imidazole containing naphthyl as an electron acceptor indicates the presence of additional charge transfer singlet states.

When TiO_2 nanoparticles were added to imidazole solution, the absorbance around 257 nm increases along with a red shift. No significant shift was observed with the bands around 233 nm and 305 nm at higher concentration of TiO_2. These changes in absorption of imidazole imply a strong electronic coupling between imidazole and TiO_2 nanoparticles. This may result in change in electronic distribution in imidazole which causes an increase in molar absorbance along with bathochromic shift due to the formation of imidazole-TiO_2 composite. The absorption characteristics of imidazole with TiO_2 have been shown in Fig. 7. The absorption of imidazole at 257 nm was shifted to 260 and 264 nm with TiO_2 (R) and TiO_2 (A), respectively, and no significant shift was detected for the bands at 233 and 305 nm. The binding strength of imidazole with nanoparticles were calculated using Benesi Hildebrand equation [94], $\frac{1}{\Delta A} = \frac{1}{A_C - A_0} + \frac{1}{K(A_C - A_0)[\text{nanoparticles}]}$, where ΔA is the change in absorbance at a fixed wavelength, A_0 and A_c are the absorbance of free sensitizer and the

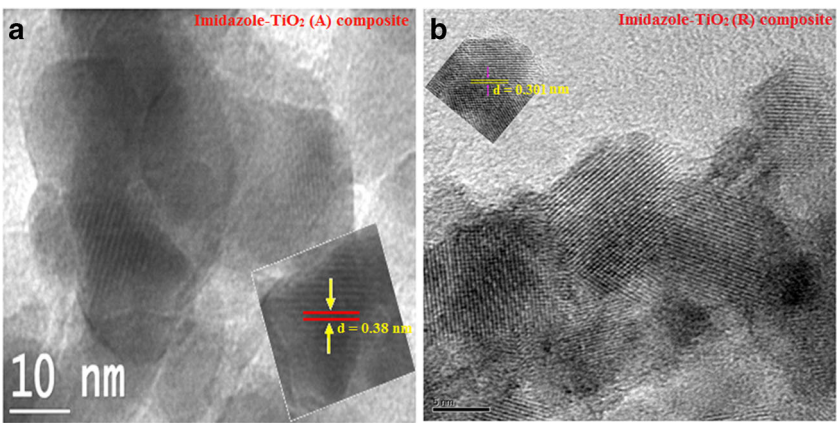

Fig. 6 TEM images of (**a**) imidazole-TiO_2 (A) composite and (**b**) imidazole-TiO_2 (R) composite

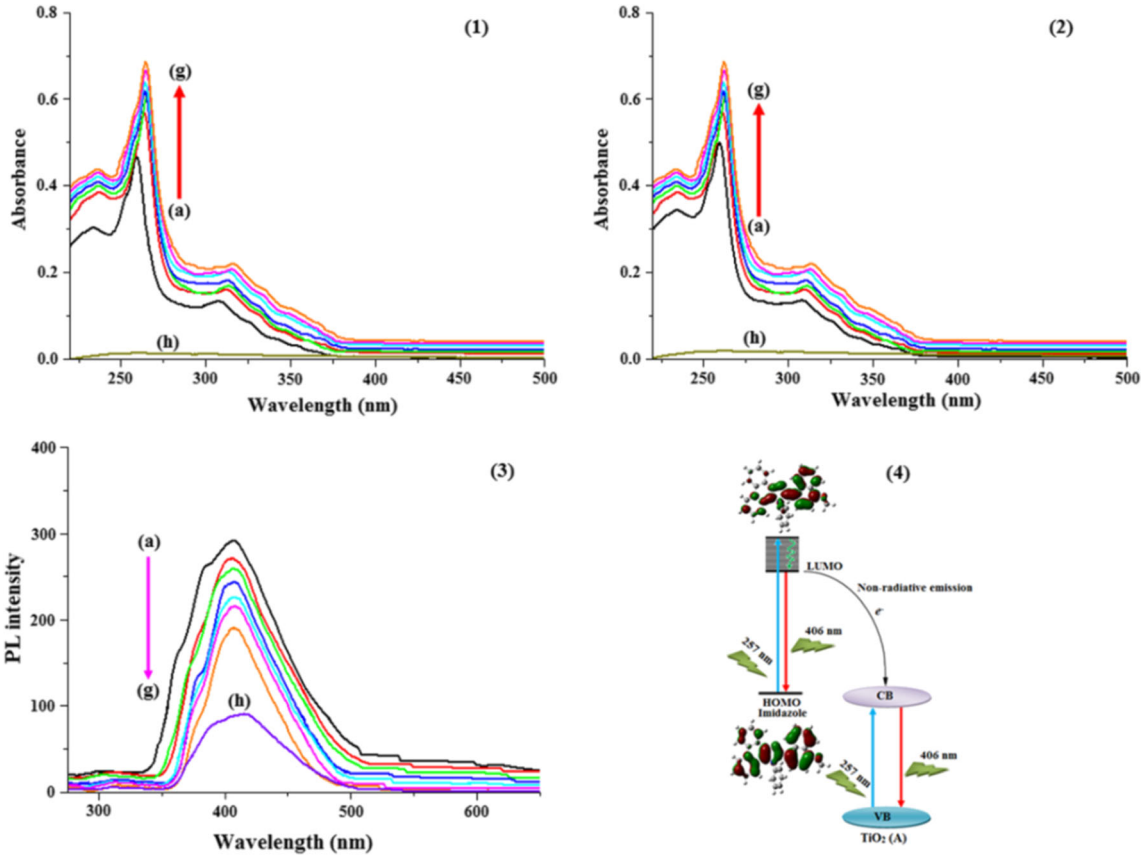

Fig. 7 **a** Absorption spectra of (**a**) 10 μM imidazole, (b→f) 10 μM imidazole with TiO_2 (A) (1) and TiO_2 (R) (2) nanoparticles (20→100 nM) and (g) TiO_2 TiO_2 (A) and TiO_2 (R) nanoparticles (100 μM); (**3**) Emission spectra of (a) 10 μM imidazole, (**b→f**) 10 nM imidazole with TiO_2 (A) nanoparticles 2→10 nM) and (g) TiO_2 (A) nanoparticles (10 nM); (**4**) Energy level diagram describing the conduction and valence bands of TiO_2 and the electron donating energy level of imidazole

composite [imidazole-nanoparticles], respectively For the composite formation a linear relationship will be obtained between $1/\Delta A$ and 1/[nanoparticles]. From the ratio of the intercept $1/(A_c - A_0)$ to the slope $1/K\,(A_c - A_0)$, the binding constant has been calculated, as 2.89×10^3 and 11.01×10^9 M^{-1} for TiO_2 (A) and TiO_2 (R), respectively. The higher K value in the presence of TiO_2 (R) nanoparticles indicates the strong binding of imidazole with TiO_2 (R).

Fluorescence Quenching by TiO_2 (A)

The effect of increasing concentration of TiO_2 (A) on the emission spectra of the imidazole is shown in Fig. 7. Addition of these nanoparticles to imidazole results in fluorescence quenching [95, 96] and the binding constant has been obtained using the following equation, $1/(F_0 - F)=1/(F_0 - F')+1/\,K\,(F_0 - F')$ [TiO_2 (A)], where F_0 is the fluorescence intensity of the bare imidazole, F' is the fluorescence intensity of the imidazole adsorbed on TiO_2 nanoparticles and F is the observed fluorescence intensity at different loading of TiO_2. The binding constant has been assessed as 3.91×10^3 M^{-1}.

The ability of the excited state imidazole to inject its electrons into the conduction band (CB) of TiO_2 nanoparticles is determined from the energy difference between the CB of TiO_2 nanoparticles and excited state oxidation potential of imidazole. Using the equation $E_{s^*/s+}=E_{s/s+}-E_s$, where, $E_{s/s+}$ is the oxidation potential of imidazole and E_s is the excited state energy the calculated oxidation potential of the excited singlet state imidazole is −2.32 V. The excited state energy of the imidazole is obtained from the fluorescence maximum based on the reported method [97]. The energy level of the CB of TiO_2 (A) nanoparticles is shown in Fig. 7 [98]. It implies that the electron transfer from excited state of imidazole to the CB of nanoparticulate TiO_2 (A) is favourable.

Fluorescence Enhancement by TiO_2 (R)

Emission spectra of imidazole in presence of TiO_2 (R) nanoparticles dispersed at different loading and also in their absence are displayed in Fig. 8. The rutile nanoparticles enhance the emission of imidazole without shifting its emission maximum (406 nm). This indicates that the rutile nanocrystals do not modify the excitation process of the imidazole. The enhanced emission observed with the dispersed rutile nanoparticles is due to the adsorption of imidazole on semiconductor surface. This is due to effective transfer of electron from the

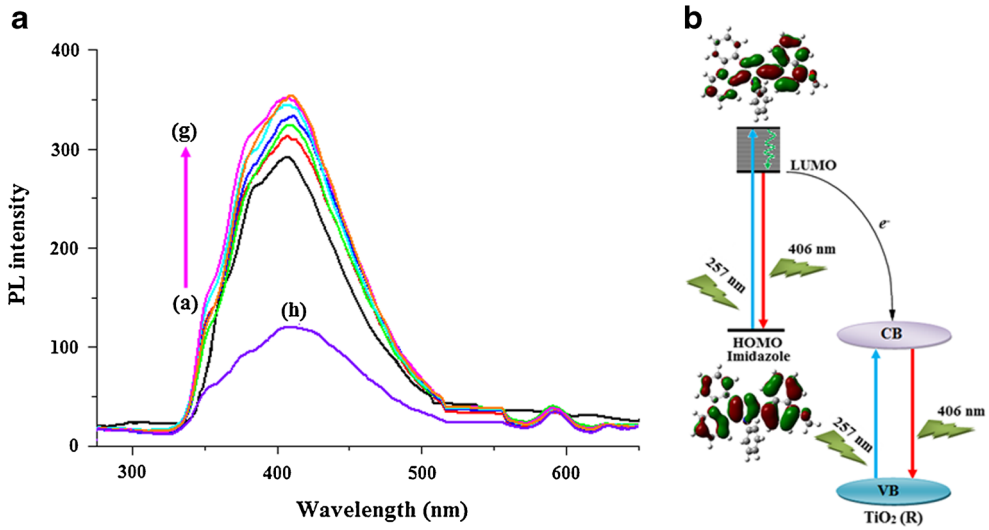

Fig. 8 Emission spectra of (**a**) 10 μM imidazole, (**b**→**f**) 10 nM imidazole with TiO_2 (R) nanoparticle 2→10 nM) and (g) TiO_2 (R) nanoparticles (10 nM) (**a**); (**b**) Enhancement of fluorescence of imidazole by TiO_2 (R) nanoparticles

excited state of the imidazole to the CB of rutile TiO_2 nanoparticles. Fluorescence enhancement arises due to the formation of imidazole-TiO_2 (R) composite. The binding constant (K) has been calculated as 10.12×10^9 M^{-1}. Such a large binding constant indicates that imidazole is strongly associated to the surface of nanocrystals by electrostatic interactions. The obtained large binding constant is because of the surface area; the surface area of the former is smaller than that of the latter. The greater interaction of smaller nanocrystals with imidazole is not only due to the large surface area of the smaller nanocrystals but also because of larger surface curvature of the smaller nanocrystals. The larger surface curvature reduces the steric hindrance between the surface binding molecules and provides a large number of unsaturated dangling bonds on the nanocrystal surface and enhances the binding interaction.

Several mechanisms for the enhancement are possible; Free energy transfer (FRET) from imidazole to nanocrystals and electron transfer from excited imidazole to the CB of nanosemiconductors. On the basis of Forster's energy transfer (FRET) formalism, there are three requirements for FRET to occur from imidazole to nanocrystals, i.e., efficient overlap between emission and absorption spectra of imidazole and nanocrystals, center-to-center distance of imidazole and nanocrystals and coupling between imidazole and nanocrystals transition dipole moments. Therefore the energy transfer efficiency is related not only to the distance between the acceptor TiO_2 and donor imidazole (r_0) but also to the critical energy transfer distance (R_0). The critical energy transfer distance (R_0), $R_0^6=8.8\times10^{-25}K^2N^{-4}\varphi J$, where, K^2 is the spatial orientation factor of the dipole, N is the refractive index of the medium, φ is the fluorescence quantum yield of the donor and J is the overlap integral of the fluorescence emission spectrum of the donor and the absorption spectrum of the acceptor. The value of J (1.05×10^{-11} [TiO_2 (R) and 1.25×10^{-11} cm^3LM^{-1} TiO_2 (A)] is calculated by using the equation, $J=\int F(\lambda)\varepsilon(\lambda)\lambda^4 d\lambda/F(\lambda)d\lambda$, where, $F(\lambda)$ is the fluorescence intensity of the donor and $\varepsilon(\lambda)$ is molar absorptivity of the acceptor. The calculated values of R_0 and r_0 are 1.78×10^{-10}, TiO_2 (R) and 1.81×10^{-9} m, TiO_2 (R) and 1.80 TiO_2 (R) and 2.47 nm TiO_2 (A), respectively. The value of K^2 (=2/3) and N (0.955) used are from the literature [28] and the φ value is from the present study. The obtained donor-acceptor distance (r_0) is consistent with the covalent attachment of imidazole with TiO_2 nanoparticles and the calculated value of R_0 is in the range of maximal critical distance. The energy transfer efficiency (E) was calculated using the formula $E=mR_0^6/(mR_0^6+r_0^6)$ where, R_0 is the critical distance when the transfer efficiency is 50 % and m is the average number of acceptor molecules interacting with one imidazole. A value of m lower than 10 was estimated on the basis of imidazole to nanocrystal concentration ratio, leading to an energy transfer efficiency lower than 0.02 for both the composites. This means that the energy transfer from imidazole to nanocrystal is negligible. Therefore, the observed enhancing and quenching is likely originated from an electron transfer process only. All these results put forward that the optoelectronic behavior of imidazole will be enhanced in the presence of TiO_2 nanoparticles which implies its potential application in the field of nanodrug carriers. Ducking of napthyl moiety in the void space of rutile TiO_2 and absence of such behaviour in the anatase, due to steric reasons, is the possible cause for the contrasting behaviour of fluorescence enhancement and quenching of imidazole by TiO_2 (R) and TiO_2 (A), respectively.

Photoelectron Transfer (PET)

The HOMO and LUMO energy levels have been calculated using the equations, $HOMO=-e(E_{ox}+4.71)$ (Ev); $LUMO=-e(E_{red}+4.71)$ (eV). On the basis of the relative

position of energy levels of isolated imidazole molecule and TiO_2 (R), it is confirmed that the electron injection is thermodynamically allowed from the excited singlet of the imidazole to the CB of TiO_2 (R). Fig. 8 presents the HOMO and LUMO energy levels of an isolated imidazole molecule along with the CB and valence band VB edges of TiO_2 (R) nanoparticles. The electron in the LUMO of the excited molecule is of higher energy than the CB of TiO_2 (R). This should lead to transfer of electron from LUMO of the excited molecule to the CB of TiO_2 (R) thereby quenching the fluorescence of imidazole. However, contrary to the expectations, enhancement of fluorescence is observed in presence of TiO_2 (R) nanocrystals. This may be because of the lowering of the HOMO and LUMO energy levels of imidazole due to the adsorption on TiO_2 (R) nanoparticles [99, 100].

The primitive tetragonal TiO_2 (R) and body centered tetragonal TiO_2 (A) crystalline structures consist of deformed TiO_6 octahedra connected differently by corners and edges. In rutile, two octahedral edges are shared to form linear chains along the 001 direction and the TiO_6 chains are linked to each other through corner shared bondings. In anatase, each octahedron shared four edges with other four octahedra, resulting in a zig - zag structure. The cross section of the void space in rutile is~4.6 Å which is the unit cell length of rutile phase. This void space permits seating of the phenanthrimidazole moiety of the imidazole comfortably. The cross section of the imidazole moiety is 4.0 Å which is less than that of the void space present in rutile. In anatase there is no such void space and also the unit cell length is not as large as that of rutile; the unit cell length in anatase is~3.8 Å. This steric restriction provides an explanation for the difference in the behaviour of binding of imidazole with these two phases. Insertion or the perfect seating of imidazole molecule in the void space of rutile allows binding of each imidazole molecule to rutile TiO_2 molecules. Since such insertion is not possible in the case of TiO_2 (A), the imidazole molecule is bound to a single site. This explains the different mode of adsorption of imidazole on the rutile and anatase phases and based on this imidazole is used to differentiate TiO_2 (R) from TiO_2 (A).

On irradiation at 250 nm, both the imidazole and TiO_2 (R) are excited. Dual emission is expected due to LUMO→HOMO and CB→VB electron transition. Also possible is electron jump from the excited imidazole to the nanocrystal; the electron in the LUMO of the excited imidazole is of higher energy compared to that in the CB of TiO_2 nanocrystals. The polar TiO_2 surface enhances the delocalisation of the π electrons and lowers the HOMO and LUMO energy levels due to adsorption [101]. The emission intensity of imidazole bound to TiO_2 (R) is far larger than that of the isolated molecule; the excited imidazole emits fluorescence at 406 nm. With the imidazole adsorbed on TiO_2 (R) the semiconductor is also excited on illumination. The recombination of the electron in the CB with the hole in the VB results in emission at 406 nm. On interaction of imidazole with TiO_2 the polar TiO_2 (R) surface enhances the delocalisation of the π electrons and lowers the HOMO and LUMO energy levels of the adsorbed imidazole due to ligand—semiconductor complex formation [102]. If the HOMO and LUMO energy levels of imidazole lowered by about 0.56 eV on complexation with TiO_2 the energy difference between LUMO and CB of TiO_2 will be about 3.05 eV. This corresponds to emission at 406 nm. The additional path opened due to LUMO→CB electron jump increase the intensity of emission at 406 nm.

Free-Energy Change (ΔG_{et}) for Electron Transfer Process

The thermodynamic feasibility of excited state electron transfer reaction has been confirmed by well known Rehm-Weller expression [103], $\Delta G_{et}=E^{1/2}{}_{(ox)}-E^{1/2}{}_{(red)}-E_s+C$, where, $E^{1/2}{}_{(ox)}$ is the oxidation potential of imidazole, $E^{1/2}{}_{(red)}$ is the reduction potential of rutile and anatase phases of TiO_2 nanoparticles, i.e., the conduction band potential of nanoparticles, E_s is the excited state energy of derivative and C is the coulombic term. Since the ligand is neutral and the solvent used is polar in nature, the coulombic term in the above expression can be neglected. The negative ΔG_{et} around −3.12 eV in both the cases indicate the thermodynamic feasibility of the electron transfer process [104, 105].

Decay Lifetime

Figure 9 displays the fluorescence decay of imidazole, the decay follows a bi-exponential fit indicating imidazole is in two excited states - one is likely to be the configuration in which the naphthyl ring is perpendicular with the phenanthrimidazole ring [excited state I] and the other is the one in which the same is coplanar with the phenanthrimidazole ring [excited state II]. The X-ray crystal structure [106] and theoretical calculation [82] show the perpendicular configuration as most stable and hence the observed longer lifetime is attributed to the same. The observed biexponential decay indicates that the imidazole composites formation is possible with the both conformation of imidazole. The perpendicular conformation of imidazole with nanoparticles is predominant than the other with planner conformation of imidazole. The radiative (k_r) and non-radiative (k_{nr}) rate constants of the excited state have been obtained using the rate constants are $k_r=\Phi/\tau$; $k_{nr}=(1/\tau)$ - (Φ/τ); $\tau=(k_r+k_{nr})^{-1}$, where Φ is quantum yield and τ is lifetime. The decrease in lifetime for the composites formation was correlated with electron transfer process. The rate constants for electron transfer process (k_{et}) from excited state of imidazole to semiconductor nanoparticles can be calculated using the equation, $k_{et}=1/\tau_{ads}-1/\tau$ (Table 1). The observed intensity enhancement and lifetime is indicative of the fact that the imidazole interaction

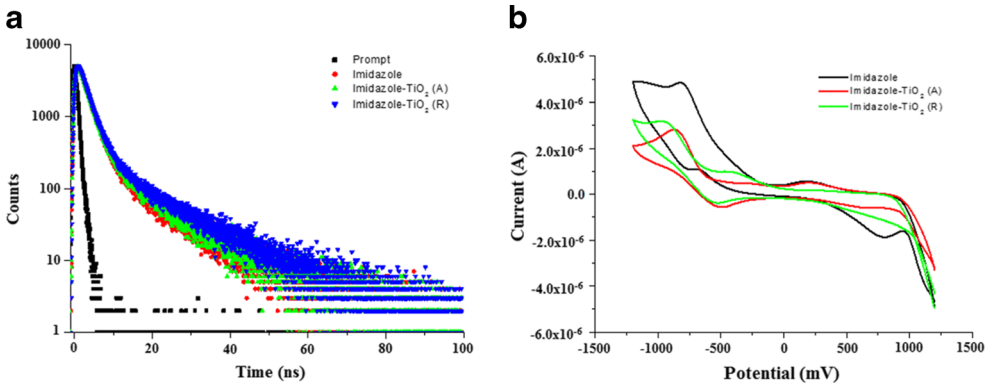

Fig. 9 **a** Fluorescence lifetime decay spectra of imidazole and imidazole-TiO_2 composites; **b** Cyclic voltammogram of imidazole along with imidazole-TiO_2 composites

with TiO_2 (R) and TiO_2 (A) nanocrystals results in energy transfer.

Evidence for Linkage

Cyclic voltametric studies were carried out to probe the efficient binding of TiO_2 (R) and TiO_2 (A) nanoparticles with imidazole. Figure 9 shows the cyclic voltammogram (CV) of imidazole, imidazole-TiO_2 (R) and imidazole-TiO_2 (A) composites. In presence of TiO_2 nanoparticles the CV of imidazole shows a shift in peak potentials along with decrease in peak current [107]. It is evident that the TiO_2 (R) and TiO_2 (A) nanoparticles have efficient binding with imidazole which supports the electronic spectral results.

The FT-IR spectra of TiO_2, imidazole and imidazole-TiO_2 composites are displayed in Fig. 10. In the case of bare TiO_2 (R) and TiO_2 (A). Ti-O stretching vibration is observed at 447 cm^{-1}. For imidazole-TiO_2 composites, C=C and C-O-C stretching vibrations are observed around 1509 and 1335 cm^{-1} in addition to the Ti-O stretching mode at 462 cm^{-1}. The frequency observed around 1600 cm^{-1} by imidazole and imidazole-TiO_2 composites corresponds to C=N function. The absorption around 3050 cm^{-1} is due to≥C-H of imidazole and imidazole-TiO_2 composites. The peak at~966 cm^{-1} is likely due to the phenyl C-H stretching.

Among the three basic sites in the imidazole the azomethine nitrogen is involved in the binding process with TiO_2 nanoparticles. This is because of the high electron density at the azomethine nitrogen. In order to prove the higher electron density at azomethine nitrogen, we have performed DFT calculation to get the molecular electrostatic potential (MEP) for imidazole, bare TiO_2 and imidazole-TiO_2 composites. The MEP map (Fig. 11) shows that nitrogen atoms represent the most negative potential region (dark red).

The predominance of green region in the MEP surface corresponds to a potential halfway between the two extremes red and dark blue colours. Mulliken charge distribution shows that titanium atom exhibits more positive charge and the azomethine nitrogen atom exhibits a more negative charge (Table S1 & S2).

Electronic Properties of TiO_2 Clusters and the Composites

The bent TiO_2 is energetically more stable by about 1.9 eV than its linear isomer. The Ti–O bond length and O– $\widehat{Ti}$ –O bond angle are 1.65 Å and 108°, respectively. The bent TiO_2 formation is explained by the interaction of Ti atom with O_2 molecule which results in a metastable structure in which the O– $\widehat{Ti}$ –O bond angle and Ti–O and O–O interatomic distances are 46.80, 1.82 and 1.47 Å, respectively. The energy of the bent structure is lower by 4.12 eV than the metastable isomer and the energy barrier between these two structures is 0.26 eV. On interaction of Ti atom with metastable TiO_2 cluster, the O–O bond is broken and planar Ti_2O_2 is formed. Ti–Ti and Ti–O bond lengths are 2.23 and 1.89 Å, respectively. The interaction of Ti_2O_2 cluster with O_2 molecule results cis and trans Ti_2O_4 clusters. Trans Ti_2O_2 is 0.28 eV lower energy than its cis isomer. The ring isomer of Ti_3O_6 is less stable than its

Table 1 Bi exponential fitting parameter for fluorescence decay of imidazole, imidazole–TiO_2 (A) and imidazole–TiO_2 (R) composites

Compound	10^2 a_1	10^9 τ_1 (ns)	10^3 a_2	10^8 τ_2 (ns)	τ_{ave} (ns)	k_r 10^{-8} s^{-1}	k_{nr} 10^{-8} s^{-1}	k_{et} 10^{-8} s^{-1}
Imidazole –TiO_2 (A) composite	3.49	2.09	1.66	1.15	2.51	1.91	2.07	1.1
Imidazole–TiO_2 (R) composite	3.61	2.14	1.29	1.23	2.49	1.93	2.09	1.3
Imidazole	3.51	2.11	1.72	1.30	2.62	1.83	1.98	1.1

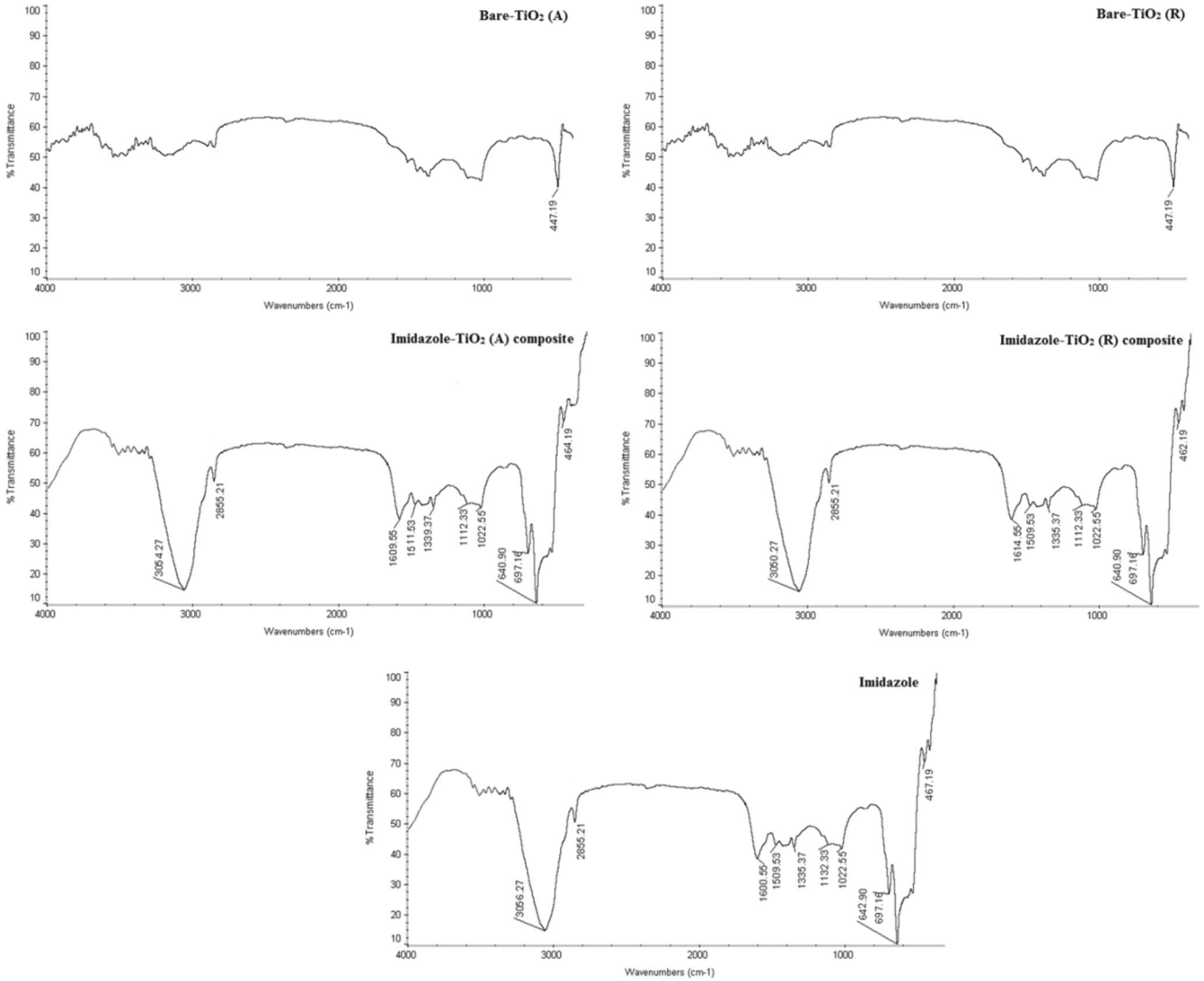

Fig. 10 FT-IR spectra of imidazole, bare TiO_2 (A) & TiO_2 (R), imidazole-TiO_2 (A) composite and imidazole-TiO_2 (R) composite

cage isomer by 1.47 eV. Similar results are obtained for Ti_4O_8 and Ti_5O_{10} clusters.

The calculated total energy per TiO_2 unit (E_T/m) (m and E_T are the number of TiO_2 units and the total energy of the cluster, respectively) is obtained as 23.61, 24.31, 24.68 and 24.92 eV for trans TiO_2, cage Ti_3O_3, cage Ti_4O_8 and cage Ti_5O_{10}, respectively. Comparison of two-dimensional (2D) clusters with the planar clusters show that all 2D clusters have a ring structure and the number of monovalent oxygen atoms is set to n and Ti atoms bind to three oxygen atoms. The energy difference $E_{diff}=E_{plnr}$ - E_{na} between the lowest lying structure of a particular cluster (E_{na}) and its planar isomer (E_{plnr}) decreases with decreasing n. The calculated positive E_{diff} shows that three-dimensional (3D) cluster structures are more stable than 2D isomers. The formation of the 2D clusters become quite unfavourable as the size of the cluster grows. For 3D clusters the formal oxidation states of oxygen and titanium atoms are (−2) and (+4), respectively. In contrast to 3D clusters, most of the oxygen and titanium atoms in the 2D clusters do not reach their formal oxidation states, which lower the stability of these planar structures. Presence of O–O repulsive interaction lowers the stability of 2D clusters. The ring radius of the planar clusters increases with n, which leads to a decrease in average interatomic distance between oxygen atoms and lowering the repulsive interaction.

We have calculated the energy gap (E_g) of the highest occupied molecular orbital (HOMO)–lowest unoccupied molecular orbital (LUMO) (Fig. 12) of all the clusters in order to elucidate the electronic properties. As a consequence of the quantum confinement effect the HOMO–LUMO gap (E_g) decreases as the material size grows. However, we have not found any correlation between E_g and size of the clusters. The calculated E_g values are much dispersed and the quantum size effect emerges from confinement. The structure of the clusters plays an important role in determining the electronic properties, since the corresponding orbitals are localized on

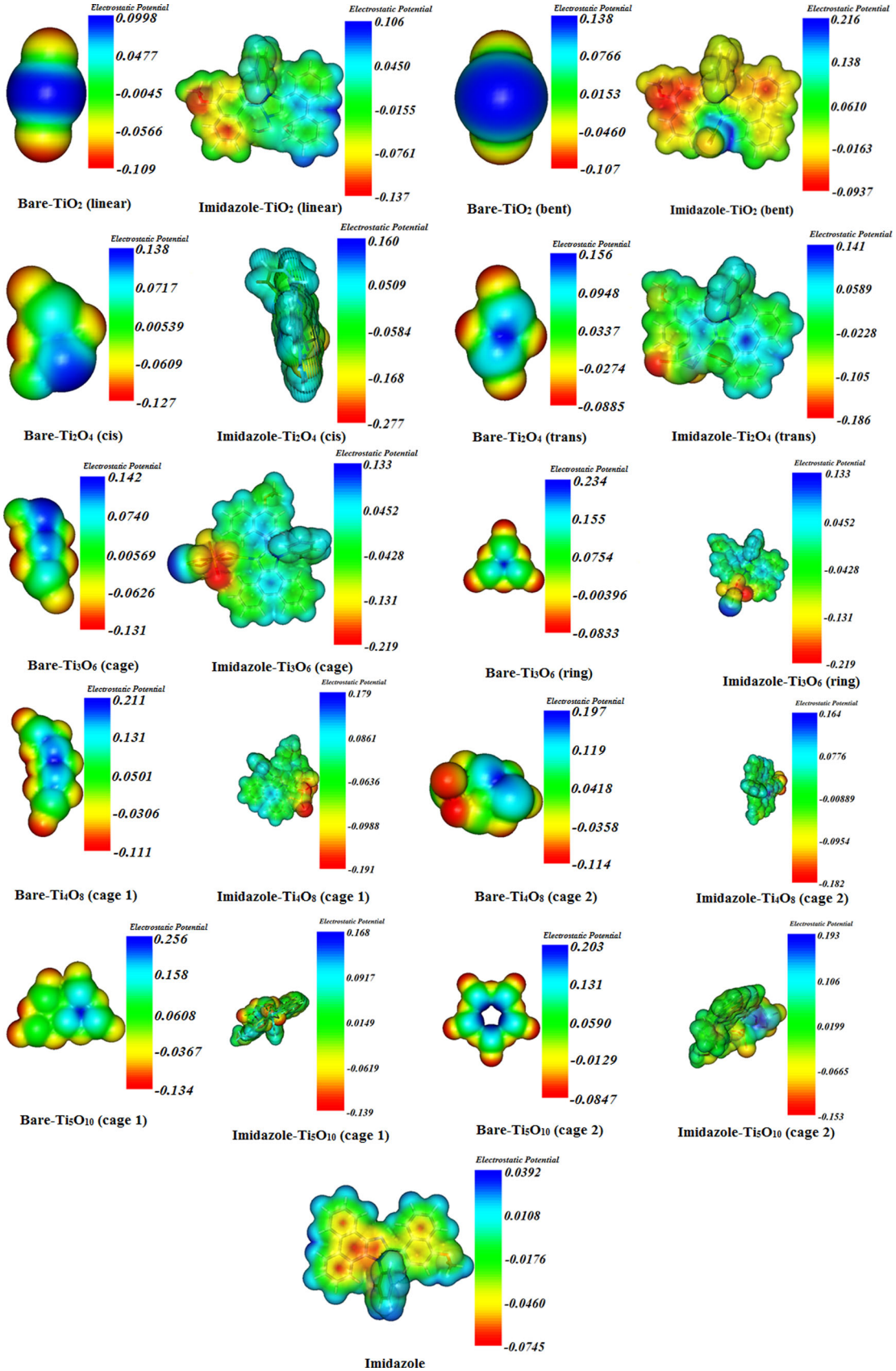

Fig. 11 Molecular electrostatic potential (MEP) diagram of bare $(TiO_2)_n$ and imidazole–Ti_nO_n composites

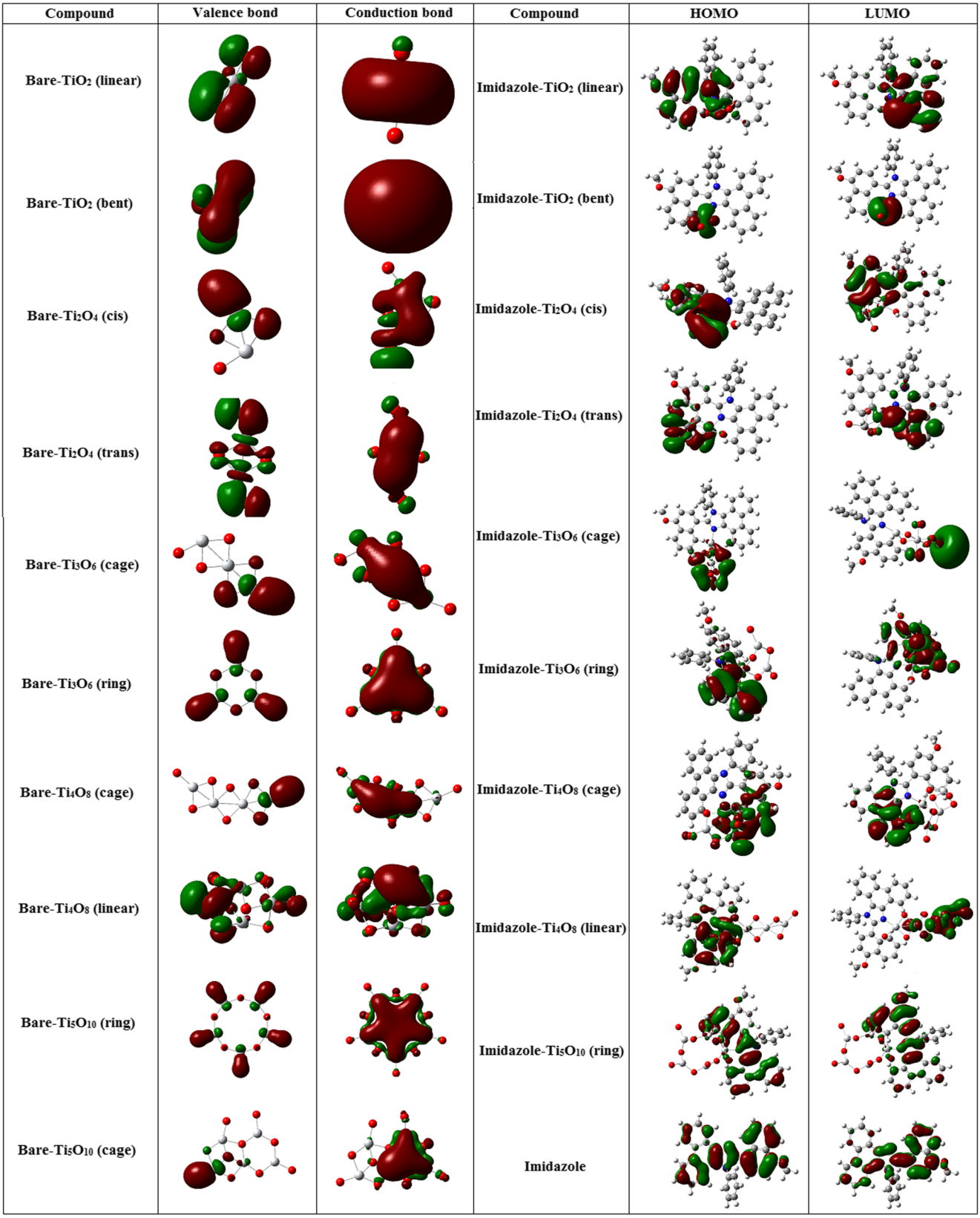

Fig. 12 HOMO-LUMO contour maps for imidazole, bare $(TiO_2)_n$ and imidazole-$(TiO_2)_n$ composites

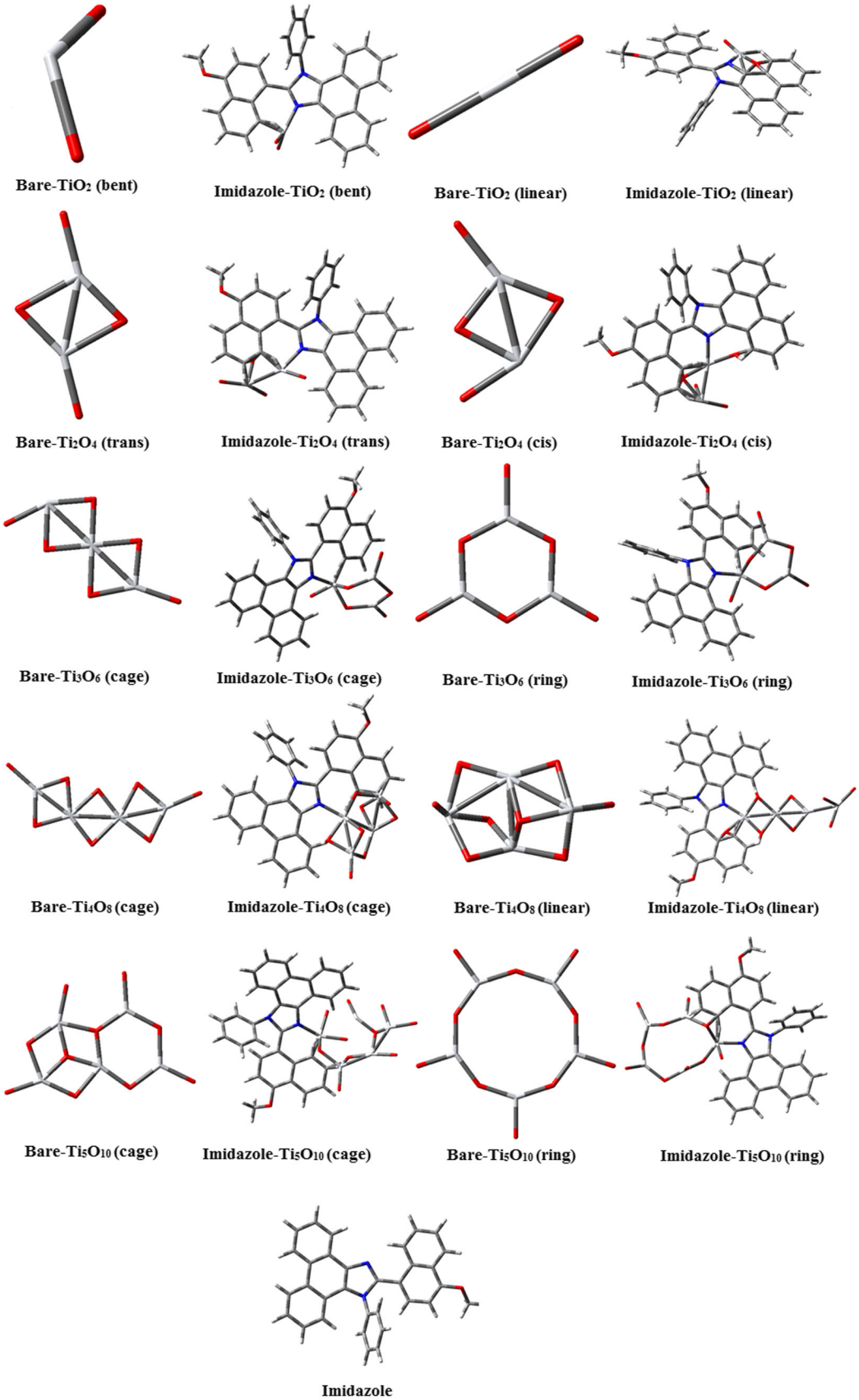

Fig. 13 Optimized structures of imidazole, bare $(TiO_2)_n$ and imidazole-$(TiO_2)_n$ composites

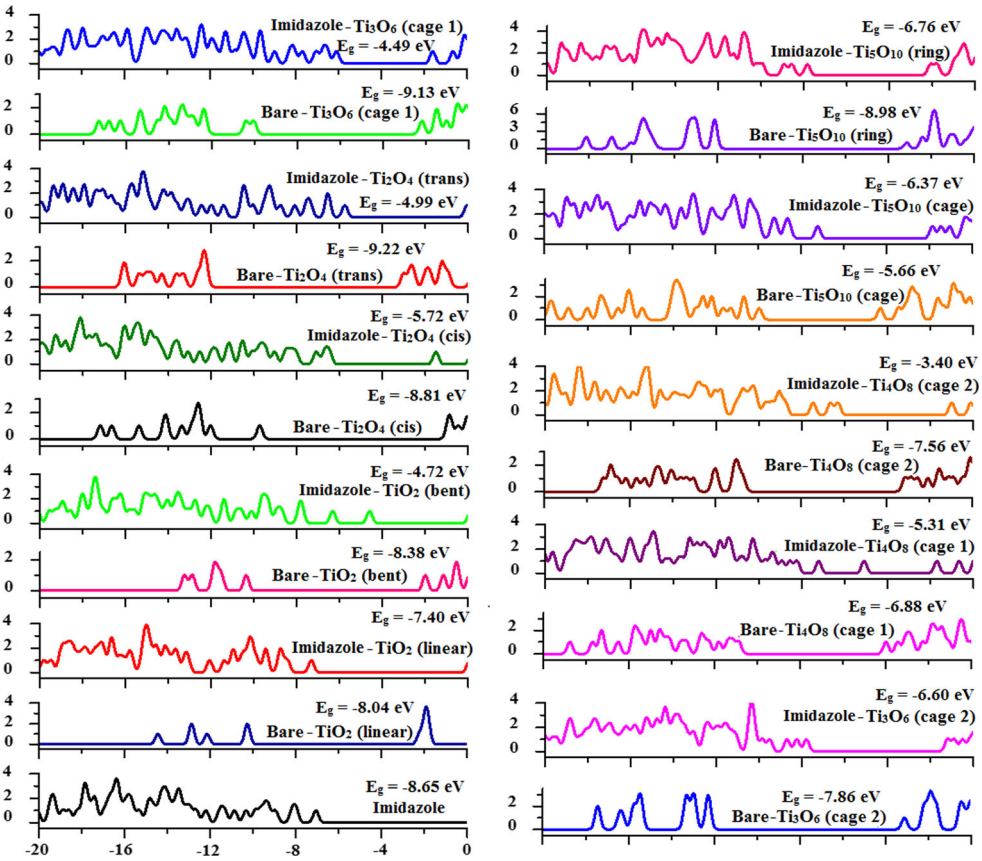

Fig. 14 Projected density of states (PDOS) for imidazole, bare $(TiO_2)_n$ and imidazole-$(TiO_2)_n$ composites

the surfaces and their energies depend on the surface structures. There is a correlation between the stability and E_g of the clusters; larger E_g implies a higher stability of a particular system. We have analysed in detail the interaction of the ground state structures of the small titania clusters with a single imidazole molecule via three different adsorption modes: molecular adsorption, dissociative adsorption and H-bonding. The optimized structures of the composites are displayed in Fig. 13. Molecular adsorption of imidazole is common for all clusters and we have observed that the imidazole molecule preferentially binds to one of the titanium atoms. But binding of the imidazole with clusters decrease energy gap as shown

Table 2 E_{HOMO}, E_{LUMO}, energy gap (E_g), distance Ti–N (Å), binding energies (E_b), optimised energies (E) and dipolemoments of imidazole–TiO_2 composites along with TiO_2 clusters

Compound	E_{HOMO}	E_{LUMO}	E_g (eV)	E_b (eV)		Ti–N	D
				N-site	O-site		
Imidazole	−7.06	1.59	−8.65	–	–	–	3.98
Imidazole-TiO_2 (linear)	−7.31 (−10.25)	0.09 (−2.21)	−7.40 (−8.04)	5.24	2.01	2.02	15.5 (1.2)
Imidazole-TiO_2 (bent)	−4.59 (−10.36)	0.13 (−1.98)	−4.72 (−8.38)	5.52	2.91	2.02	16.65 (8.9)
Imidazole-Ti_2O_4 (cis)	−5.75 (−9.72)	−0.03 (−0.91)	−5.72 (−8.81)	7.06	2.82	2.01	23.3 (8.82)
Imidazole-Ti_2O_4 (trans)	−6.48 (−12.23)	−1.49 (−3.01)	−4.99 (−9.22)	7.66	3.02	2.01	27.0 (0.00)
Imidazole-Ti_3O_6 (ring)	−7.79(−10.00)	−1.19 (−2.14)	−6.60 (−7.86)	7.19	3.20	2.02	18.03 (0.00)
Imidazole-Ti_3O_6 (cage)	−6.09 (−12.21)	−1.6 (−3.08)	−4.49 (−9.13)	7.34	2.62	2.02	10.54 (9.80)
Imidazole-Ti_4O_8 (cage 1)	−6.31 (−10.86)	−1.0 (−3.98)	−5.31 (−6.88)	7.86	2.56	2.01	32.34 (5.4)
Imidazole-Ti_4O_8 (cage 2)	−5.09 (−10.71)	−1.69 (−3.15)	−3.40 (−7.56)	7.89	2.42	2.01	29.06 (3.5)
Imidazole-Ti_5O_{10} (ring)	−7.83 (−12.12)	−1.07 (−3.14)	−6.76 (−8.98)	7.75	3.56	2.02	28.07 (0.00)
Imidazole-Ti_5O_{10} (cage)	−7.22 (−10.0)	−0.85 (−4.34)	−6.37 (−5.66)	7.80	3.89	2.02	24.40 (9.1)

values in the parenthesis corresponds to theoretical values

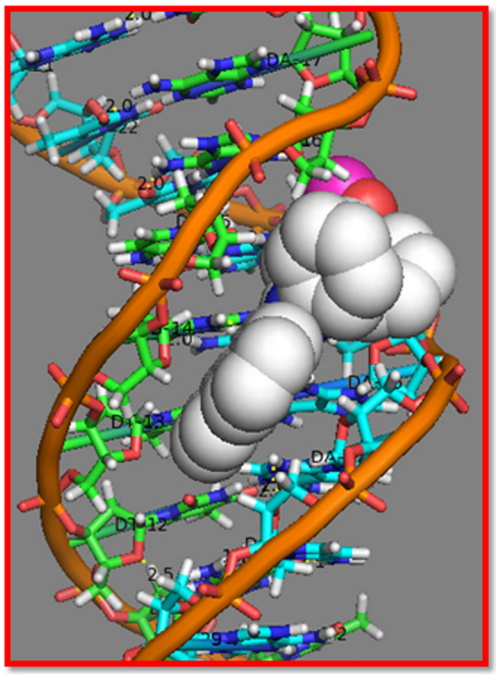

Fig. 15 Molecular docked model of 2-(4-methoxynaphthalen-1-yl)-1-phenyl-1H-phenanthro[9.10-d]imidazole located within the DNA

by Fig. 13. This is due to the effective overlap of *d*-orbital if the titanium with the lone pair of the azomethine nitrogen atom.

The projected density of states (PDOS) for the composites is presented in Fig. 14. The bare TiO_2 DOS spectra contains a broad VB and a broad CB, separated by a wide bandgap. The PDOS shows that the energies of LUMO from the isolated adsorbate and the edge of the CB coinsides and therefore the LUMO of the composite contains contribution from both adsorbate and substrate. The adsorbate LUMO coupled with CB of TiO_2 and is spread over significant portion of the substrate CB. The calculated dipolemoment of the composite is relatively larger than that of bare imidazole and (TiO_2)n clusters due to the rearrangement of electron density upon the formation of imidazole-TiO_2 composites. Due to the stronger interaction of the lone electron pairs of the nitrogen atom with the titania cluster the interatomic distance between the titanium and nitrogen atoms is around 2.01 Å. The binding energy (E_b) has been calculated using the equation, $E_b = E_T[(TiO_2)n] + E_T$ [imidazole]- E_T [composite]; E_b values ranging from 1.35 to 1.03 eV for the TiO_2 clusters. The magnitude and shape of HOMO and LUMO levels and energy gap (E_g) have strong effects on the reactivity and chemical stability of a material. Similar to electronic properties of the bare clusters, the structure of the binding sites of the imidazole molecule and the structure of the clusters influence the interaction strength as displayed in Table 2. The change in the E_g of the odd n clusters upon adsorption of the imidazole molecule are larger than those of the even n clusters [74]. Adsorption of imidazole on clusters causes the magnetization of the composites with induced magnetic moments. If the cluster size decreases, the ground state energy increases because the surface to volume ratio becomes high. The surface atoms have a lower coordination in smaller cluster and average number of bond is lower. The surface energy contributes to the ground state energy and becomes high in odd clusters which are of ionic nature the even clusters are of covalent nature and the even clusters are more stable than odd clusters.

Table 3 Binding interaction energies of 2-(4-methoxynaphthalen-1-yl)-1-phenyl-1H-phenanthro[9.10-d]imidazole with DNA

Conformation	Binding Affinity (Kcal/mol)
1	−9.5
2	−9.2
3	−8.8
4	−8.7
5	−8.6
6	−8.5
7	−8.4
8	−8.2
9	−8.0
10	−7.8

Molecular Docking Studies

To understand the binding interaction between biological macromolecule with 2-(4-methoxynaphthalen-1-yl)-1-phenyl-1H-phenanthro[9.10-d]imidazole for the rational drug design and drug discovery molecular docking study has been carried out. By placing the 2-(4-methoxynaphthalen-1-yl)-1-phenyl-1H-phenanthro[9.10-d]imidazole into the binding site of the target specific region of the DNA mainly in a non-covalent fashion and to predict the correct binding mode and binding affinities [108]. The more negative the binding energy the stronger is the interaction between the 2-(4-methoxynaphthalen-1-yl)-1-phenyl-1H-phenanthro[9.10-d]imidazole and DNA, the most stable the complex formed between 2-(4-methoxynaphthalen-1-yl)-1-phenyl-1H-phenanthro[9.10-d]imidazole and DNA.

In our experiment, the 2-(4-methoxynaphthalen-1-yl)-1-phenyl-1H-phenanthro[9.10-d]imidazole were successively docked with DNA duplex of sequence d(CGCGAATT CGCG)2 dodecamer (PDB ID: 1BNA) in order to expect the selected binding site along with favored orientation of the drug inside the DNA groove. The energetically favorable conformation of the docked pose exposed that 2-(4-methoxynaphthalen-1-yl)-1-phenyl-1H-phenanthro[9.10-d]imidazole binds to groove of DNA (Fig. 15). From the results (Table 3), it can be found that the binding free energy (DG) is apparently lower when there are adenine (A) and thymine (T) base pairs in the DNA sequences, indicating that

the preferential binding site of 2-(4-methoxynaphthalen-1-yl)-1-phenyl-1H-phenanthro[9.10-d]imidazole on the A-T rich sequence of DNA. However, 2-(4-methoxynaphthalen-1-yl)-1-phenyl-1H-phenanthro[9.10-d]imidazole prefers to bind on the minor groove of A-T rich region of DNA molecule, which is reliable with above experimental results, and the considerable change of conformation of 2-(4-methoxynaphthalen-1-yl)-1-phenyl-1H-phenanthro[9.10-d]imidazole occurs in the binding process with DNA to orient easily along the minor groove.

Conclusion

Fluorescent enhancement of imidazole by rutile TiO_2 and quenching by anatase TiO_2 have been explained and binding constants have been obtained based on photoelectron transfer (PET) mechanism; the negative ΔG_{et} values reveal that the electron transfer process is thermodynamically favourable. SEM with EDX, TEM and electronic spectral analyses show the adsorption of imidazole on the TiO_2 surface. We have studied the stability, structural and electronic properties of the bare $(TiO_2)_n$ clusters of different sizes and their interaction with imidazole. The calculated HOMO–LUMO orbital energies and their differences, exhibit geometry and size dependence and do not follow a regular pattern. The interaction between the imidazole and TiO_2 clusters is dominated by the hybridization between *d*-orbitals of titanium and *p*-orbital of the azomethine nitrogen atom and this determines the strength of interaction of imidazole with TiO_2. The interaction strength between imidazole molecule and the ground state structure of a particular cluster depends on the size of the cluster. Adsorption of the imidazole on the TiO_2 clusters modifies the electronic properties of the TiO_2 clusters and the HOMO–LUMO analysis confirms the occurrence of charge transfer. Mulliken charge distribution shows that titanium atom exhibits more positive charge and the azomethine nitrogen atom exhibits a more negative charge. These two atoms form the weak interaction of Ti–N bond (N-site) in imidazole– TiO_2 composites. The calculation reveals reduction in the energy gap for imidazole-TiO_2 composite compared to the bare TiO_2 and imidazole. Docking analysis shows that 2-(4-methoxynaphthalen-1-yl)-1-phenyl-1H-phenanthro[9.10-d]imidazole prefer to bind on the minor groove of A-T rich region of DNA molecule.

Acknowledgments One of the authors Prof. J. Jayabharathi is thankful to DST (No. SR/S1/IC-73/2010), DRDO (NRB-213/MAT/10-11), UGC (F. No. 36-21/2008 (SR)) and CSIR (NO 3732/NS-EMRII) for providing funds to this research study.

References

1. Diebold U (2003) The surface science of titanium dioxide. Surf Sci Rep 48:53–229
2. Thompson TL, Yates JT (2006) Surface science studies of the photoactivation of TiO_2-new photochemical processes. Chem Rev 106:4428–4453
3. Chen X, Mao SS (2007) Titanium dioxide nanomaterials: synthesis, properties, modifications, and applications. Chem Rev 107: 2891–2959
4. O'Regan B, Grätzel M (1991) A low-cost, high-efficiency solar cell based on dye-sensitized colloidal TiO_2 films. Nature 353:737–740
5. Grätzel M (2001) Photoelectrochemical cells. Nature 414:338–344
6. Grätzel M (2003) Dye-sensitized solar cells. J Photochem Photobiol C 4:145–153
7. Hagfeldt A, Grätzel M (1995) Light-induced redox reactions in nanocrystalline systems. Chem Rev 95:49–68
8. Cakir D, Gulseren O, Mete E, Ellialtioglu S (2009) Dye adsorbates BrPDI, Br Gly, and Br Asp on anatase TiO2 (001) for dye-sensitized solar cell applications. Phys Rev B 80:035431
9. Wu NL, Wang SY, Rusakova IA (1999) Inhibition of crystallite growth in the sol–gel synthesis of nanocrystalline metal oxide. Science 285:1375–7
10. Agrios AG, Pichat P (2005) State of the art and perspectives on materials and applications of photocatalysis over TiO_2. J Appl Electrochem 35:655–63
11. Hoffmann MR, Martin ST, Choi W, Bahnemann DW (1995) Environmental applications of semiconductor photocatalysis. Chem Rev 95:69–96
12. Fujishima A, Honda K (1972) Electrochemical photolysis of water at a semiconductor electrode. Nature 238:37–8
13. Fujishima A, Hashimoto K, Watanabe H (1997) TiO_2 photocatalysis: fundamentals and applications. BKC, Tokyo
14. Wang R, Hashimoto K, Fujishima A, Chikuni M, Kojima E, Kitamura A, Shimohigoshi M, Watanabe T (1997) Light-induced amphiphilic surfaces. Nature 388:431–2
15. Sunada K, Kikuchi Y, Hashimoto K, Fujishima A (1998) Bactericidal and detoxification effects of TiO_2 thin film photocatalysts. Environ Sci Technol 32:726–8
16. Cakir D, Gulseren O (2009) Phys Rev B80:125424
17. Anpo M, Shima T, Kodama S, Kubokawa Y (1987) Photocatalytic hydrogenation of CH@3^CCH with H@2^O on small-particle TiO@2^: Size quantization effects and reaction intermediates. J Phys Chem 91:4305–10
18. McIntyre NS, Thompson KR, Weltner W (1971) Spectroscopy of titanium oxide and titanium dioxide molecules in inert matrices at 4.deg.K. J Phys Chem 75:3243–9
19. Balducci G, Gigli G, Guido M (1985) Mass spectrometric study of the thermo chemistry of gaseous $EuTiO_3$ and TiO_2. J Chem Phys 83:1909–12
20. Balducci G, Gigli G, Guido M (1985) Identification and stability determination of the gaseous Titanium Oxides molecules Ti_2O_3 and Ti_2O_4. J Chem Phys 83:1913–6
21. Yu W, Freas RB (1990) Formation and fragmentation of gas-phase titanium/oxygen cluster positive ions. J Am Chem Soc 112:7126–7133
22. Guo BC, Kerns KP, Castleman AW (1992) J Mass Spectrom Ion Process 117:129–144
23. Chertihin GV, Andrews L (1995) Reactions of laser ablated titanium, zirconium, and hafnium atoms with oxygen molecules in condensing argon. Phys Chem 99:6356–6366

24. Wu H, Wang LS (1997) Electronic structure of titanium oxide clusters: TiO_y (y=1–3) and $(TiO_2)_n$ (n=1–4). J Chem Phys 107: 8221–8228
25. Foltin M, Stueber GJ, Bernstein ER (1999) On the growth dynamics of neutral vanadium oxide and titanium oxide clusters. J Chem Phys 111:9577–9586
26. Matsuda Y, Bernstein ER (2005) On the titanium oxide neutral cluster distribution in the Gas phase: detection through 118 nm single - photon and 193 nm multiphoton ionization. J Phys Chem A 109:314–319
27. Zhai HJ, Wang LS (2007) Probing the electronic structure and band Gap evolution of titanium oxide clusters $(TiO_2)_n^-$ (n=1–10) using photoelectron spectroscopy. J Am Chem Soc 129: 3022–3026
28. Hagfeldt A, Bergstrom R, Siegbahn HOG, Lunell S (1993) Structure and stability of small titanium/oxygen clusters studied by ab initio quantum chemical calculations. J Phys Chem 97: 12725–12730
29. Bergstrom R, Lunell S, Eriksson LA (1996) Comparative study of DFT methods applied to small titanium/oxygen compounds. Int J Quantum Chem 59:427–443
30. Walsh MB, King RA, Schaefer HF (1999) The structure, electron affinities and energetic stabilities of TiO_n and TiO_n – (n=1,3). J Chem Phys 110:5224–5230
31. Albaret T, Finocchi F, Noguera C (1999) First principles simulations of titanium oxide clusters and surfaces. Faraday Discuss 114: 285–304
32. Albaret T, Finocchi F, Noguera C (1999) Ab initio simulation of titanium dioxide clusters. Appl Surf Sci 144/145:672–676
33. Albaret T, Finocchi F, Noguera C (2000) Density functional study of stoichiometric and O-rich titanium oxygen clusters. J Chem Phys 113:2238–2249
34. Jeong KS, Chang C, Sedlmayr E, Sulze D (2000) Electronic structure investigation of neutral titanium oxide molecules Ti_xO_y. J Phys B: At, Opt Phys 33:3417–3430
35. Hamad S, Catlow CRA, Woodley SM, Lago S, Mejias JA (2005) Structure and stability of small TiO_2 nanoparticles. J Phys Chem B 109:15741–15748
36. Woodley AM, Hamad S, Mejias JA, Catlow CRA (2006) Properties of small TiO_2, ZrO_2 and HfO_2 nanoparticles. J Mater Chem 16:1927–1933
37. Qu ZW, Kroes GJ (2006) Theoretical study of the electronic structure and stability of titanium dioxide clusters (TiO2)n with n=1–9. J Phys Chem B 110:8998–9007
38. Qu ZW, Kroes GJ (2007) Theoretical study of stable, defect-free (TiO_2)(n) nanoparticles with n=10–16. J Phys Chem C 111: 16808–16817
39. Persson P, Gebhardt JCM, Lunell S (2003) The smallest possible nanocrystals of semiionic oxides. J Phys Chem B 107:3336–3339
40. Lundqvist MJ, Nilsing M, Persson P, Lunell S (2006) DFT study of bare and dye-sensitized TiO_2 clusters and nanocrystals. Int J Quantum Chem 106:3214–3234
41. Barnard AS, Erdin S, Lin Y, Zapol P, Halley JW (2006) Modeling the structure and electronic properties of TiO_2 nanoparticles. Phys Rev B73:205405
42. Li S, Dixon DA (2008) Molecular structures and energetics of the (TiOâ)n (n=1–4) clusters and their anions. J Phys Chem A 112: 6646–6666
43. Calatayud M, Maldonado L, Minot C (2008) Reactivity of $(TiO_2)_N$ clusters (N=1-10): probing gas-phase acidity and basicity properties. J Phys Chem C 112:16087–16095
44. Calatayud M, Minot C (2009) Is there a nanosize for the activity of TiO_2 compounds? J Phys Chem C 113:12186–12194
45. Bandyopadhyay I, Aikens CM (2011) Structure and stability of $(TiO_2)_n$, $(SiO_2)_n$, and mixed $Ti_mSi_{n-m}O_{2n}$ [n=2–5, m=1 to (n−1)] clusters. J Phys Chem A 115:868–879
46. Syzgantseva OA, Navarrete PG, Calatayud M, Bromley S, Minot C (2011) Theoretical investigation of the hydrogenation of (TiO_2)(N) clusters (N=1–10). J Phys Chem C 115:15890–15899
47. Chiodo L, Salazar M, Romero AH, Laricchia S, Sala FD, Rubio A (2011) Structure, electronic, and optical properties of TiO_2 atomic clusters: an ab initio study. J Chem Phys 135:244704
48. Marom N, Kim M, Chelikowsky JR (2012) Structure selection based on high vertical electron affinity for TiO_2 clusters. Phys Rev Lett 108:106801
49. Koparde VN, Cummings PT (2005) Molecular dynamics simulation of titanium dioxide nanoparticle sintering. J Phys Chem B 109:24280–24287
50. Naicker PK, Cummings PT, Zhang H, Banfield JF (2005) Characterization of titanium dioxide nanoparticles using molecular dynamics simulations. J Phys Chem B 109:15243–15249
51. Hoang VV (2007) Structural properties of simulated liquid and amorphous TiO_2. Phys State Solidi 244:1280–1287
52. Shevlin SA, Woodley SM (2010) Electronic and optical properties of doped and undoped $(TiO_2)_n$Nanoparticles. J Phys Chem C 114: 17333–17343
53. Hush NS (1985) Distance dependence of electron transfer rates. Coord Chem Rev 64:135–157
54. Marcus RA (1989) Relation between charge transfer absorption and fluorescence spectra and the inverted region. J Phys Chem 93: 3078–3086
55. Gould IR, Young RH, Moody RE, Farid S (1991) Contact and solvent-separated geminate radical ion pairs in electron-transfer photochemistry. J Phys Chem 95:2068–2080
56. Gould IR, Noukakis D, Jahn LG, Young RH, Goodman JL, Farid S (1993) Radiative and nonradiative electron transfer in contact radical-ion pairs. J Chem Phys 176:439–456
57. Cortes J, Heitele H, Jortner J (1994) Band-shape analysis of the charge-transfer fluorescence in barrelene-based electron donor-acceptor compounds. J Phys Chem 98:2527–2536
58. deLaszlo SE, Hacker C, Li B, Kim D, Maccoss M, Mantle N, Pivnichny JV, Colwell L, Koch GE, Cascieri MA, Hagmann WK (1999) Potent, orally absorbed glucagon receptor antagonists. Bioorg Med Chem Lett 9:641–646
59. Eyers PA, Craxton M, Morrice N, Cohen P, Goedert M (1998) Conversion of SB 203580-insensitive MAP kinase family members to drug-sensitive forms by a single amino-acid substitution. Chem Biol 5:321–328
60. Newman MJ, Rodarte JC, Benbatoul KD, Romano SJ, Zhang C, Krane S, Moran EJ, Uyeda RT, Dixon R, Guns ES, Mayer LD (2000) Discovery and characterization of OC144-093, a novel inhibitor of P-glycoprotein-mediated multidrug resistance. Cancer Res 60:2964–2972
61. Antolini M, Bozzoli A, Ghiron C, Kennedy G, Rossi T, Ursini A (1999) Analogues of 4,5-bis(3,5-dichlorophenyl)-2-trifluoromethyl-1H-imidazole as potential antibacterial agents. Bioorg Med Chem Lett 9:1023–1028
62. Black JW, Durant GJ, Emmett JC, Ganellin CR (1974) Sulphur-methylene isosterism in the developent of metiamide, a new histamine H_2-receptor antagonist. Nature 248:65–67
63. Uçucu Ü, Karaburun NG, Işikdağ İ (2001) Synthesis and analgesic activity of some 1-benzyl-2-substituted-4,5-diphenyl-1H-imidazole derivatives. Farmaco 56:285–290
64. Wang L, Woods KW, Li Q, Barr KJ, McCroskey RW, Hannick SM, Gherke L, Credo RB, Hui YH, Marsh K, Warner R, Lee JY, Zielinski-Mozng N, Frost D, Rosenberg SH, Sham HL (2002) Potent, orally active heterocycle-based combretastatin A-4 analogues: synthesis, structure-activity relationship, pharmacokinetics, and in vivo antitumor activity evaluation. J Med Chem 45: 1697–711
65. Maier T, Schmierer R, Bauer K, Bieringer H, Buerstell H, Sachse B (1989) US patent 4820335. Chem Abstr 111:1949w

66. Siddiqui SA, Narkhede UC, Palimkar SS, Daniel T, Lahoti RJ, Srinivasan KV (2005) Room temperature ionic liquid promoted improved and rapid synthesis of 2,4,5-triaryl imidazoles from aryl aldehydes and 1,2-diketones or α-hydroxyketone. Tetrahedron 61: 3539–3546
67. Heravi MM, Zakeri M, Karimi N, Saeedi M, Oskooie HA, Hosieni NT (2010) Acidic ionic liquid [(CH_2) $4SO_3HMIM][HSO_4$]: a green media for the simple and straightforward synthesis of 2,4, 5-trisubstituted imidazoles. Synth Commun 40:1998–2006
68. Wang J, Mason R, VanDerveer D, Feng K, Bu XR (2003) Convenient preparation of a novel class of imidazo[1,5-a]pyridines: decisive role by ammonium acetate in chemoselectivity. J Org Chem 68:5415–5418
69. Sarshar S, Siev D, Mjalli MM (1996) Imidazole libraries on solid support. Tetrahedron Lett 37:835–838
70. Gallagher TF, Seibel GL, Kassis S, Laydon JT, Blumenthal MJ, Lee JC, Lee D, Boehm JC, Fier-Thompson SM, Abt JW, Soreson ME, Smietana JM, Hall RF, Garigipati RS, Bender PE, Erhard KF, Krog AJ, Hofmann GA, Sheldrake PL, McDonnell PC, Kumar S, Young PR, Adams JL (1997) Regulation of stress-induced cytokine production by pyridinylimidazoles; inhibition of CSBP kinase. Bioorg Med Chem 5:49–64
71. Shaabani A, Rahmati A (2006) Silica sulfuric acid as an efficient and recoverable catalyst for the synthesis of trisubstituted imidazoles. J Mol Catal A Chem 249:246–248
72. Kantevari S, Vuppalapati SVN, Biradar DO, Nagarapu L (2007) Highly efficient, one-pot, solvent-free synthesis of tetrasubstituted imidazoles using $HClO_4 – SiO_2$ as novel heterogeneous catalyst. J Mol Catal A Chem 266:109–113
73. Kidwai M, Mothsra P, Babsal V, Goyal R (2006) Efficient elemental iodine catalyzed One-Pot synthesis of 2,4,5-triarylimidazoles. Monatsh Chem 137:1189–1194
74. Nilsing M, Persson P, Ojamäe L (2005) Anchor group influence on molecule–metal oxide interfaces: periodic hybrid DFT study of pyridine bound to TiO_2 via carboxylic and phosphonic acid. Chem Phys Lett 415:375–380
75. Li Q, Chen X, Wang X, Zhao Y, Ma F (2000) Ionic self-assembled wormlike nanowires and their cyclodextrin inclusion-tuned transition. J Phys Chem B 104:10384–10390
76. De Angelis F, Tilocca A, Selloni A (2004) Time-dependent DFT study of [Fe(CN)(6)](4-) sensitization of TiO_2 nanoparticles. J Am Chem Soc 126:15024–15025
77. Persson P, Lundqvist MJ (2005) Calculated structural and electronic interactions of the ruthenium Dye N3 with a titanium dioxide nanocrystal. J Phys Chem B 109:11918–11924
78. Persson P, Lundqvist MJ, Ernstorfer R, Goddard WA, Willig FJ (2006) Quantum chemical calculations of the influence of anchor-Cum-spacer groups on femtosecond electron transfer times in dye-sensitized semiconductor nanocrystals. J Chem Theory Comput 2: 441–451
79. Persson P, Lunell S, Ojamae L (2002) Electronic interactions between aromatic adsorbates and metal oxide substrates calculated from first principles. Chem Phys Lett 364:469–474
80. Nilsing M, Lunell S, Persson P, Ojamae L (2005) Phosphonic acid adsorption at the TiO_2 anatase (1 0 1) surface investigated by periodic hybrid HF-DFT computations. Surf Sci 582:49–60
81. Rajh T, Nedeljkovic JM, Chen LX, Poluektov O, Thurnauer MC (1999) Improving optical and charge separation properties of NanocrystallineTiO2 by surface modification with vitamin. J Phys Chem B 103:3515–3519
82. Mennucci B, Cossi M, Scalmani G, Rega N, Petersson GA, Nakatsuji H, Hada M, Ehara M, Toyota K, Fukuda R, Hasegawa J, Ishida M, Nakajima T, Honda Y, Kitao O, Nakai H, Klene M, Li X, Knox JE, Hratchian HP, Cross JB, Bakken V, Adamo C, Jaramillo J, Gomperts R, Stratmann RE, Yazyev O, Austin AJ, Cammi R, Pomelli C, Ochterski JW, Ayala PY, Morokuma K, Voth GA, Salvador P, Dannenberg JJ, Zakrzewski VG, Dapprich S, Daniels AD, Strain MC, Farkas O, Malick DK, Rabuck AD, Raghavachari K, Foresman JB, Ortiz JV, Cui Q, Baboul AG, Clifford S, Cioslowski J, Stefanov BB, Liu G, Liashenko A, Piskorz P, Komaromi I, Martin RL, Fox DJ, Keith T, Al-Laham MA, Peng CY, Nanayakkara A, Challacombe M, Gill PMW, Johnson B, Chen W, Wong MW, Gonzalez C, Pople JA (2004) Gaussian, Inc., Wallingford CT
83. Nikkanen J, Kanerva T, Mantyla T (2007) The effect of acidity in low-temperature synthesis of titanium dioxide. J Cryst Growth 304:179–183
84. Cheng H, Ma J, Zhao Z, Qi L (1995) Hydrothermal preparation of uniform nanosize rutile and anatase particles. Chem Mater 7:663–671
85. Ojha PK, Roy K (2010) Chemometric modeling, docking and in silico design of triazolopyrimidine-based dihydroorotate dehydrogenase inhibitors as antimalarials. Eur J Med Chem 45:4645–4656
86. Morris GM, Goodsell DS, Halliday RS, Huey R, Hart WE, Belew RK, Olson AJ (1998) Automated docking using a Lamarckian genetic algorithm and an empirical binding free energy function. J Comput Chem 19:1639–1662
87. Morris GM, Huey R, Lindstrom W, Sanner MF, Belew RK, Goodsell DS, Olson AJ (2009) AutoDock4 and AutoDockTools4: automated docking with selective receptor flexibility. J Comput Chem 30:2785–2791
88. Huey R, Morris GM, Olson AJ, Goodsell DS (2007) A semiempirical free energy force field with charge-based desolvation. J Comput Chem 28:1145–1152
89. De Lano WL (2004) The PyMOL molecular graphics system. De Lano Scientific, San Carlos
90. Yin WJ, Chen S, Yang JH, Gong XG, Yan Y, Wei SH (2010) Effective band gap narrowing of anatase TiO_2 by strain along a soft crystal direction. Appl Phys Lett 96:221901
91. Karunakaran C, Gomathisankar P (2003) Solvothermal synthesis of CeO_2-TiO_2 nanocomposite for visible light-photocatalytic detoxification of cyanide. ACS Sustainable Chem Eng 1:1549–1555
92. Czerwieniec R, Herbich J, Kapturkiewicz A, Nowacki J (2000) Radiative electron transfer in planar donor-acceptor quinoxaline derivatives. Chem Phys Lett 325:589–598
93. Gudipati MS, Daverkausen J, Maus M, Hohlneicher G (1944) Higher electronically excited states of phenanthracene, carbazole and fluorine. Chem Phys 186:289–301
94. Benesi HA, Hildebrand JH (1949) A spectrophotometric investigation of the interaction of iodine with aromatic hydrocarbons. J Am Chem Soc 71:2703–2707
95. Hou J, Huo L, He C, Yang C, Li Y (2006) Synthesis and absorption spectra of poly(3-(phenylenevinyl)thiophene)s with conjugated side chains. Macromolecules 39:594–603
96. Kathiravan A, Anbazhagan V, Asha Jhonsi M, Renganathan R (2008) Fluorescence quenching of *meso*-tetrakis (4-sulfonatophenyl) porphyrin by colloidal TiO_2. Spectrochim Acta, Part A 70:615–618
97. Shin EJ, Kim D (2002) Substituent effect on the fluorescence quenching of various tetraphenylporphyrins by ruthenium tris(2, 2′-bipyridine) complex. J Photochem Photobiol A Chem 152:25–31
98. Murov L, Carmichael I, Hug GL (1993) Handbook of photochemistry, 2nd edn. Dekker, Inc, New York, pp 269–273
99. Thanikachalam V, Arunpandiyan A, Jayabharathi J, Ramanathan P (2014) Photophysical properties of the intramolecular excited charge-transfer states of π-expanded styryl phenanthrimidazoles – effect of solvent polarity. RSC Adv 4:6790–6806
100. Nagarajan N, Velmurugan G, Prabhu G, Venuvanalingam P, Renganathan R (2014) A combined experimental and theoretical investigation of imidazole–carbazole fluorophores. J Lumin 147: 111–120

101. Hwang GT, Son HS, Ku JK, Kim BH (2003) Synthesis and photophysical studies of bis-enediynes as tunable fluorophores. J Am Chem Soc 125:11241–11248
102. Libby WF (1963) Electron transfer among the transition elements; the controlling role of the Franck—condon principle on rates. J Chem Phys 38:420
103. Kavarnos GJ, Turro NJ (1986) Photosensitization by reversible electron transfer: theories, experimental evidence, and examples. Chem Rev 86:401–449
104. Parret S, Savary FM, Fouassier JP, Ramamurthy P (1994) Spin—orbit-coupling-induced triplet formation of triphenylpyrylium ion: a flash photolysis study. J Photochem Photobiol A 83:205–209
105. Nath S, Pal H, Palit DK, Sapre AV, Mittal JP (1998) Steady-state and time-resolved studies on photoinduced interaction of phenothiazine and 10-methylphenothiazine with chloroalkanes. J Phys Chem A 102:5822–5830
106. Jayabharathi J, Thanikachalam V, Venkatesh Perumal M, Srinivasan N (2012) Synthesis, crystal structure, Kamlet-Taft and Catalan solvatochromic analysis of novel imidazole derivatives. J Fluoresc 22:409–417
107. Wang X, Zhang R, Wu C, Dai Y, Song M, Gutmann S, Gao F, Lv G, Li J, Li X, Guan Z, Fu D, Chen B (2007) The application of Fe_3O_4 nanoparticles in cancer research: a new strategy to inhibit drug resistance. J Biomed Mater Res A 80A:852–860
108. Haq I, Ladbury J (2000) Drug–DNA recognition: energetics and implications for design. J Mol Recognit 13:188–197